Segmentation of Proximal Femur in 3D Magnetic Resonance Images for Detection of Cam Type FAI

by

Sadaf Arezoomandershadi

A THESIS SUBMITTED IN PARTIAL FULFILLMENT OF
THE REQUIREMENTS FOR THE DEGREE OF

MASTER OF COMPUTER SCIENCE
in
School of Electrical Engineering and Computer Science
Faculty of Engineering

UNIVERSITY OF OTTAWA

This thesis is lovingly dedicated to my mother, Elham and Mehdi who supported me at the each step of the way.

Acknowledgement

I owe my deepest gratitude to Dr. WonSook Lee for providing me the opportunity to follow my research interests and this work would not have been possible without her continuous concern and exceptional support and advice. It is also an honor for me to thank Dr. Kawan Rakhra for his invaluable guidance and inspirational discussions in this study. Furthermore, I would also like to thank Dr. Paul Beaulé for his useful comments and collaboration. Finally, I share the credit of my work with my family who never failed to give me financial and moral supports.

Table of Contents

List of Figures

List of Tables

Acronyms

2D	Two Dimensional
3D	Three Dimensional
CT	Computed Tomography
FAI	Femoro-Acetabular Impingement
GT	Ground Truth
MRI	Magnetic Resonance Imaging
PDM	Parametric Deformable Model
RBF	Radial Basis Function
ROI	Region Of Interest

Abstract

Segmentation of osseous structures from clinical MR images has remained a challenging task for many years now due to inevitable acquisition artifacts and inhomogeneous intensity of bones. To come up with the associated challenges, we devised a novel parametric deformable model framework for segmentation of 3D magnetic resonance (MR) images in computer-aided diagnosis (CAD) of cam type femoro-acetabular impingement (FAI). Our framework has two phases: (i) we introduce radial basis function (RBF) interpolation for semi-automatic piecewise registration of a proximal femur atlas model to the region of interest (ROI) using landmarks displacements and (ii) a parametric deformable model for coarse-to-fine level segmentation based on acting internal and external forces. We tested our segmentation scheme on a 3D synthetic image data as well as clinical datasets of MR hip images with different resolutions and validated the results of real data in comparison with three related parametric deformable model techniques. Accordingly, we found our methodology to be robust against artifacts and intensity inhomogeneity existing in high and low-resolution images and relatively resistant to under- and over- segmentation problems.

CHAPTER 1

Introduction

1.1. Motivation

Hip joint is described as a ball-shaped bone (femoral head) that fits into the socket (acetabulum) of pelvis held by the muscles and ligaments. The area between the bones is lubricated by a smooth protein substance called cartilage to ease the painless movements in all directions. The most common cause of stiffness and severe pain in the joint is a degenerative joint disease known as osteoarthritis (OA) which features the breakdown or loss of cartilage. Research show that the major cause of hip OA is associated with a condition called femoro-acetabular impingement (FAI). In these cases, a total arthroplasty is required in order to treat the abnormalities of cartilage, resurfacing the damaged ends of the bones and improving the range of motion. Considering the resurfacing arthroplasty, the surgeon has to rub certain amount of bone in particular directions to deform the bone; in serious situations, an artificial bone is implanted during a surgical treatment.

There are various complications with total hip arthroplasty such as nerve or blood vessel damage, infection, dislocation or leg length difference. Moreover, the benefits of the artificial materials do not often last for more than 10-15 years and the surgery has to be repeated. Therefore, it is highly desired to preserve as much the natural bone as possible. The effort not only reduces the risk of surgery repetition but also decreases healthcare expenses.

Predisposing abnormalities can be detected non-invasively through various radiological imaging techniques. Antero-posterior (AP) and lateral radiographs are often considered as the first choice to investigate into symptoms of FAI. X-ray images can visually depict the gross anatomy of the hip, specifically the bone structures. However, they are only 2D, and may not be adequate to provide detailed information about the complex three-dimensional geometries of the hip. Computed tomography (CT) can provide high-resolution images, with cross-sectional capability allowing for three-dimensional multiplanar reconstructions of the bone structures of the joint. However, CT provides limited assessment of the soft tissues such as the labrum,

muscle, and hyaline cartilage. A major concern associated with CT imaging is the relatively high radiation exposure for the patient. Magnetic resonance imaging (MRI) is an imaging modality with multiplanar image acquisition capability, and strong contrast resolution, but does not impart any radiation to the patient. Thus, MRI is the preferred modality for FAI evaluation [1].

While manual analysis of a series of two-dimensional MR images is strenuous and time-consuming, employing appropriate computer-assisted image analysis techniques rather than manual investigation into images can facilitate quick and efficient processing of enormous volumes of datasets.

1.2. Objective and Organization of the Thesis

The aim of this study is to develop a 3D interactive segmentation framework to address the aforementioned issues. The effort is specifically focused on providing detailed knowledge femur in diagnosis of cam type impingement by means of transferring the shape information from an atlas model to the personalized data.

The proposed framework combines a parametric deformable model (PDM) segmentation technique with radial basis function deformation for semi-automatic initialization of the model to the image. The system is composed of two general phases:

- The first phase considers deformation of 3D model in physical space. Expressly, the model is deformed without any knowledge of the image. Hence, the deformation acts as a piecewise registration.
- The second phase uses image for refining the segmentation by means of parametric deformation of registered model in an elastic scheme. The location of the piecewise-registered model is estimated in the image domain; then, the model is deformed under the effect of the forces from the image.

Before entering the technical description of the framework, we provide background information in support of material of the thesis in the second chapter. Then we focus on the current methods of MR image segmentation explaining the benefits and ill effects of each approach in the third chapter. The chapter also covers the overview of the deformable models and their variations. Fourth chapter is composed of the supporting theory of the components of the framework and the partial goal of each component. Finally, in chapter 5 we present the

implementation and the results of the acquired as well as quantitative evaluation of the system on synthetic and MR images and compare our results with the outcome of similar methods.

1.3. Contribution

Outstanding contributions of our research are as follows:

- *Development of a 3D segmentation framework;* our 3D segmentation framework is robust against artifacts and intensity inhomogeneity existing in high and low resolution images and relatively resistant to leakage into adjacent tissues. Specifically, a 3D parametric deformable model in the second phase can facilitate the direct delineation of smooth surfaces and preserving the coherency between image slices.
- *Introduction of a thresholded balloon force to external forces;* opposing to classical parametric model, we introduce a thresholded balloon force in addition to gradient-based force for model refinement in the second phase in order to constrain inflation of the model towards the edges of the ROI.
- *Application to the model in segmentation of MR images of hip joint for cam –type impingement detection;* the segmentation framework is able to handle unavoidable inhomogeneity artifacts and spurious edges in MR images. In particular, for segmentation of MR images of hip it can evolve towards the outline of the bone i.e. cortical bone rather than getting attracted towards the edges of spongy bone.

CHAPTER 2

Background

2.1. Hip Joint

Hip joint is a ball-and-socket joint formed by convex (head of femur) and concave (acetabulum) bones. In order to avoid the abutment of the two bones during the movement, the surfaces of the bones are covered by a slippery material called articular cartilage allowing a pain-free motion. Another type of hip cartilage is labrum that is extended along the rim of socket and its function is to increase the depth of acetabulum by approximately 25% to absorb shocks and stabilize the hip joint by distributing the pressure evenly across the socket [2].

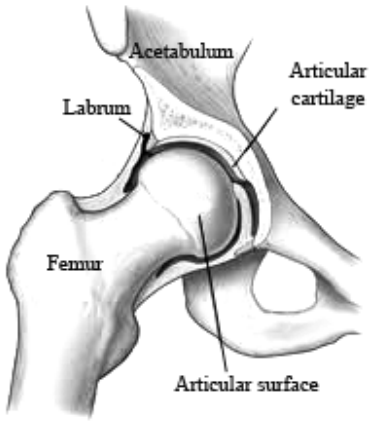

Figure 2.1. Hip joint side view

2.2. Femur

The femur (thighbone) is the strongest, longest, and heaviest bone in the body. In terms of shape, the femur is not completely vertical and the spherical head is attached to the tubular part by an arced piece of bone, corresponding to breadth of pelvis that aids in lining the knee joint with the center of the mass of body. The bone is divided into three general areas:

- *Proximal extremity;* it articulates with acetabulum to form hip joint;
- *Distal extremity;* it forms the knee joint with tibia and patella;
- *Shaft;* it is the medial part of the bone connecting the two extremities.

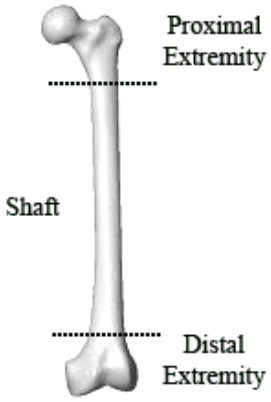

Figure 2.2. General sections of femur

2.2.1. Proximal Extremity

The proximal extremity is divisible to *head, neck, lesser and greater trochanter* and two bony ridges called *intertrochanteric line* and *intertrochanteric crest*.

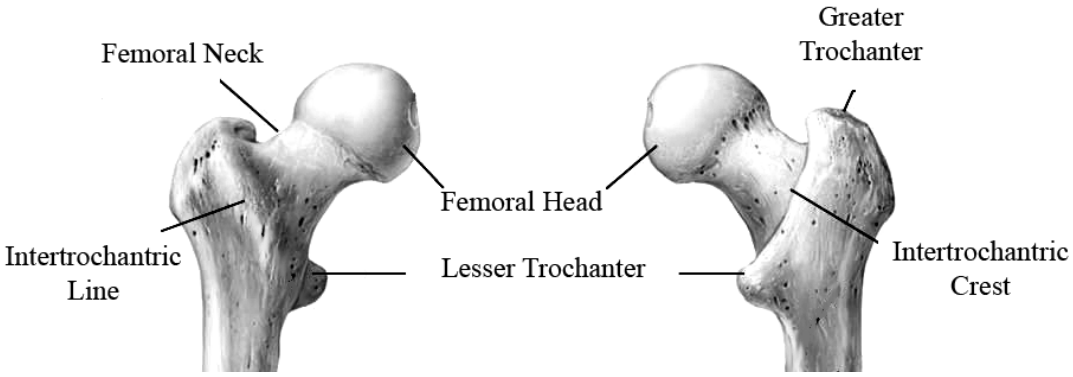

Figure 2.3. Proximal extremity

2.2.1.1 The Head (Caput Femoris)

The head is a round-shaped convex bone inclined upward and a little forward coated with cartilage except over a small depression below and behind the center of the head namely *Fovea Capitis Femoris* [3]. Although the general shape of the head is hemispherical, it has a conchoidal shape in some individuals [2].

2.2.1.2 The Neck (Callum Femoris)

The neck is a hyperbolical process of bone connecting the head with the trochanters and creating an upward angle. The angle, affecting the range of motion, is widest in infancy and decreases during growth but after that period, it does not usually have any significant change. In an adult, the average is about 125° though it varies with gender, height of the bone and width of the pelvis. The neck also has a forward angle that is usually about 12°-14° [3].

2.2.1.3 The Greater Trochanter (Trochanter Major)

The greater trochanter is a projection of the bone connecting the neck to the shaft directed lateralward and backward in an adult. It is located about one cm lower than the head [3]. In terms of shape, this section of bone is convex and quadrilateral and its function is to attach several muscles of the posterior hip and the anterior thigh. These muscles collectively are responsible for rotation, abduction, stretching and lifting the thigh sideways.

2.2.1.4 The Lesser Trochanter (Trochanter Minor)

The lesser trochanter is a conical eminence originated in the lower back part of base of the neck [3]. The projection of the bone is significant since two flexor hip muscles are emanated in lesser trochanter. The size of the process is on average about one-tenth of the femoral head.

2.2.1.5 The Intertrochanteric Line

The intertrochanteric line is a ridge of the bone that connects the two trochanters on anterior surface of the femur. A strong ligament of the hip joint is attached to femur through intertrochanteric line.

2.2.1.6 The Intertrochanteric Crest

The intertrochanteric crest is a prominent ridge of the bone connecting lesser and greater trochanters on the posterior surface. There is a small ridge in the middle of the intertrochanteric crest called *Linea Quadrata* that gives attachment to a strong abductor and rotator muscle [3].

2.3. Osteoarthritis

Osteoarthritis refers to a chronic joint disease accompanied by inflammation of the joints. It is a widespread clinical syndrome and most common type of arthritis affecting more than three million Canadians [4]. The disease is a dynamic process that has impact on all joint tissues including cartilage, bones, ligaments and muscles. The key pathological features are localized loss of cartilage and altering the structure of the adjacent bones under repetitive mechanical stimulation and new bone formation known as *osteophyte* at the contact areas [5].

Osteoarthritis is not a single disorder but it is considered as a multiple risk factor disease. These factors are extensively categorized into three groups:

- *Genetic factors*; although the genes carrying the disorder are mainly unknown, research indicates that the genetic inheritance increases the risk of disorder occurrence to 40-60%.
- *Constitutional factors*; factors such as female sex, early menopause, high density of bones increase the disorder risk. However, the most common constitutional factor that raises the OA prevalence and affects a majority of Canadians by the age of 70 is aging [4].
- *Obesity* is another significant factor that according to Arthritis Foundation, for every one extra pound added to the weight, six pounds of pressure is added to the hip joint.
- *Biomechanical risk factors*; occupational or recreational joint trauma, muscle weakness and joint stress, injury or misalignment are factors that alter the joints in a biomechanical manner [5];

There are two types of OA associated with the aforementioned risk factors; *primary OA* informally known as “wear and tear OA” is diagnosed when the reason for pain and swelling is unknown. This type of OA is generally related to the aging and the research reveals that all old people suffer from OA to some extent. On the contrary, *secondary OA* is caused by all other risk factors that often develop gradually during lifetime. The most important cause of hip secondary OA is a condition known as femoro-acetabular impingement (FAI), a syndrome that often affects young and middle-aged individuals [6].

2.4. Femoro-acetabular Impingement (FAI)

Femoro-acetabular Impingement (FAI) is a pathological condition occurring due to a mismatch between femur and acetabulum. The damage to labrum leads to injuries in acetabular cartilage and progression into osteoarthritis. At present, two classes of FAI are identified:

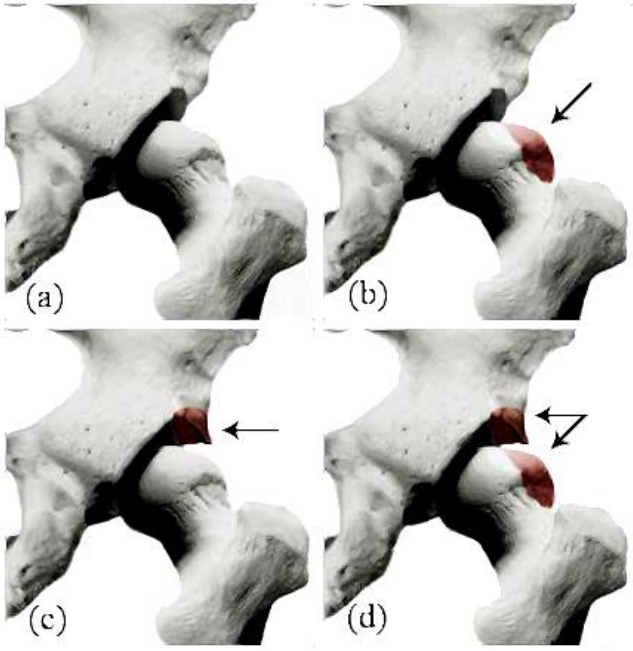

Figure 2.4. Femoro-acetabular impingement (a) Normal hip joint (b) Cam FAI (c) Pincer FAI (d) Mixed FAI

- *Cam type*; it is associated with the lesions in femoral head-neck junction and is most common among young male athletes; the mechanism involves the creation of a ridge on the surface of the femur such that the anterior femoral head-neck offset is reduced [2]. The flexion induces stress and causes the compression of the cartilage; the cartilage shrinks inwards leaving the surface of the excess part of the femur uncovered. Consequently, the femoral head is rubbed to the acetabulum rim abnormally [7].
- *Pincer type*; it describes the abnormality on the acetabulum rim and is more prevalent among middle-aged women; the acetabulum rim grows irregularly to cover a larger surface of the anterior femoral head; thereafter, limits the range of motion [7].

In some patients a combination of the two types are observed which is termed as *mixed type;*

The main symptom of FAI is pain in front hip and groin. The pain is often provoked due to prolonged activities such as sitting or walking or after any activities stimulating the joints such as doing exercises. It is believed that many people are naturally potential for FAI i.e. the investigations show that even in the normal people a minor cam or pincer type deformities can be seen. Hence, the sports professionals or people having serious mechanical activities are even more exposed to suffer from FAI.

2.4.1. FAI Diagnosis

FAI is often diagnosed with one of the following procedures:

- *History*; it involves the patient's complaint of hip pain or decreased range of motion especially adduction, flexion and internal rotation. However, most patients do not recall a specific incident urging the pain in hip joint and diagnosis based on plain history cannot be effective while can provide basic information for other tests [7].
- *Physical examination*; it consists of a series of tests to confirm the history and assessing the reasons of hip pain:
    - *The impingement test*; it includes passive flexion of the hip to 90º, slightly adduction of the hip and applying an internal rotation force in supine state [7]; so, the restrictions in the range of motion appear during the test.
    - *Flexion Abduction External Rotation (FABER) test*; the test is performed with the patient supine and the hip passively flexed, externally rotated and abducted. Then the distance of the affected knee from the examination couch is compared to the unaffected side; the greater distance implies the impingement [7].
    - *Posterior inferior impingement test*; with the patient prone, the affected hip is passively extended and externally rotated. The test is positive if the similar pain reported by the patient is evoked [2].
- *Imaging test;* over the past 10 years, improvements in imaging techniques have made non-invasive imaging methods to be widely applied in detection of FAI. However, some of the techniques are more frequently used than the others;

- *Plain radiology*; anteroposterior (AP) X-rays of pelvis and lateral X-rays of hip are often considered as the first step to determine the evidences of FAI. The images are used to extract some measurements:
    - *Head-neck offset*; the measurement is defined as the difference between the anterior radius of the femoral head and anterior radius of the femoral neck in lateral view; the normal offset is on average 9.3 mm and a value less than 7 mm indicates cam impingement [2].
    - *Alpha angle*; the angle is defined as the angle between the line passing the center of the neck and the line connecting the center of the head to the point where the head sphericity ends. The mean alpha angle for a normal is 42º-47º and in cam type impingement, it grows to 65º-70º [2]. The angle can also be measured in CT and MRI scans.
    - *Triangular index*; the index is calculated by measuring half of the head radius (r) on the neck axis and drawing a line perpendicular to the neck axis in the measured point. The new radius (R) is defined as the distance between the head center and the point of intersection between the perpendicular line and femoral head-neck contour [6]. The significant difference between r and R reveals a cam impingement.
    - *Extrusion index*; the index is defined as the percentage of the part of the femur head lateral to the acetabulum divided by total horizontal width of femoral head [8]. The percentage more than 25% implies a pincer impingement [6].

  The bottom line for choosing X-ray method prior to other image modalities is that the capturing process is quick and cost-effective. On the other hand, X-ray images are 2D, thus they may not be reliable for further studies and cannot be used for confirmation of bone and cartilage morphologies in FAI.
- *Computed Tomography (CT) scanning*; CT scans are beneficial for assessing the shape of the bone by facilitating the 3D surface reconstruction from a set of axial images; although the perceived images can provide detailed information and the imaging procedure takes only a few minutes, CT scan is rarely used for FAI

diagnosis. In addition to the risk of high dose radiation exposure, CT scans can only demonstrate the bony impingement lesion; therefore, in most diagnosis procedures, MR imaging is preferred in order to promote the visualization of soft tissue injuries [2].

- *Magnetic Resonance Imaging (MRI)*; the features of MRI has made it an appropriate technique to be routinely used in FAI diagnosis [1]. Next section covers the detailed aspects of magnetic resonance images.

Other methods of imaging such as ultrasonography and bone scintigraphy can also be applied in FAI diagnosis; however, they are scarcely referenced in literature and routine clinical assessments.

2.5. Magnetic Resonance Imaging (MRI)

Foundation of MR imaging goes back to about 70 years ago when the effect of magnetism and radio waves on the atoms were discovered. However, the first patent of MR scanning was released about 40 years ago by Raymond Damadian [10]. In MR scanning an external magnetic field is used to make the protons line up in the direction of the field. Examples of the atoms whose nuclei is influenced by an external magnetic field includes hydrogen, oxygen, carbon, nitrogen, sodium and phosphorous. Given the fact that approximately 99% of the human body is made up of hydrogen, carbon and oxygen, imposing a magnetic field to the body affects almost all atoms within the body. However, the most commonly used chemical element in magnetic resonance imaging is hydrogen. The support for this choice comes from the fact that about 99.98% of the hydrogen atoms do not contain neutrons in their nuclei and it can provide relatively strong MR signals.

Figure 2.5. MR image acquisition machine (source: http://commons.wikimedia.org/wiki/File:MRI-Philips.JPG)

The image acquisition process involves bursting radio waves towards the body in order to change the state of the protons. Once the radio wave burst is turned off, the protons return to their initial state and the realignment causes the emission of radio waves from the atoms. The amount of atoms is, however, variant in different tissues which produces contrast for distinguishing the tissues from each other on the basis of the transmitted signal. The signal is then detected by a scanner and analyzed by a computer. Unfortunately, the perceived signals are often corrupted which leave artifacts in the acquired image.

There are several sources of the artifacts most of which are related to patient or operating conditions. Knowledge about these artifacts is useful in order to avoid misjudgments in pathologies. Two of the most important factors that degrade the quality of perceived data are intensity inhomogeneity and partial volume effect that are discussed in next subsections.

2.5.1. Intensity inhomogeneity (IIH)

Intensity inhomogeneity (IIH) refers to reduced signal intensity that creates spurious smooth shades over the tissues. The effect is regarded as an obstacle for accurate statistical analysis of absolute intensity and a misleading factor in segmentation and registration procedures. The main reasons of intensity inhomogeneity are categorized in four classes that are subject to hardware and biological features [11]:

- Scanner magnetic field abnormalities;
- Biological susceptibility e.g. metal implants;
- Inappropriate positioning of the anatomy of interest;
- Scanner anomalies i.e. hardware conditions

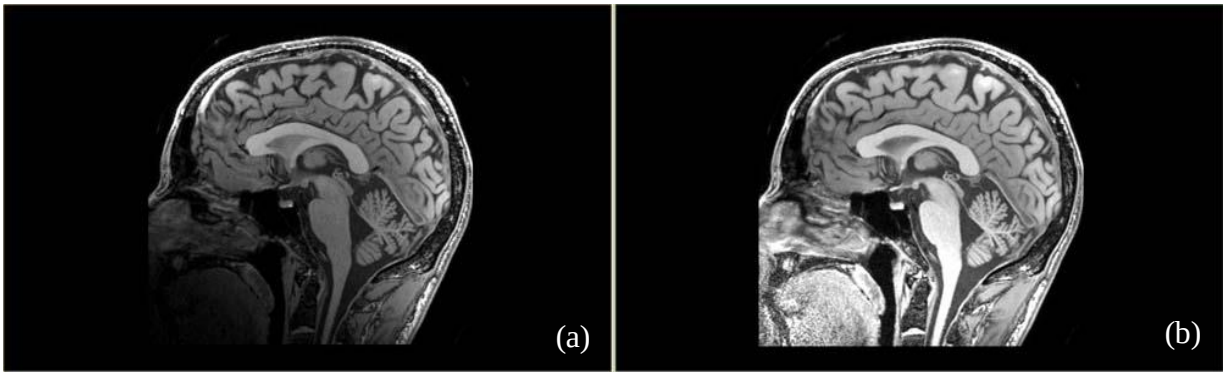

Figure 2.6. Intensity inhomogeneity correction by applying third image model (a) inhomogeneous image (b) corrected image (source: http://www.slicer.org/slicerWiki/index.php/Modules:MRIBiasFieldCorrection-Documentation-3.5)

Several methods have been addressed in literature for the purpose of IIH removal. The bottom line for the effect elimination is to model the image in terms of bias field, noise and uncorrupted image and the simplest way to model IIH is to consider it as an additive or multiplicative function; i.e. the effect is the result of addition or multiplication of the intensity value with an explicit value. Furthermore, it is essential to embody noise as an influential factor in the quality of the image. In most cases, noise is considered to have Rice or Gaussian distributions; essentially, the models should be applied on the image area and the background pixels/voxels should be excluded from all processes. There are three frequent patterns for modeling intensity inhomogeneous images; the most common model assumes that the noise is independent of bias field and is subject to the receiver device:

$$I = FU + \eta \tag{2.1}$$

where I is the corrupted image, U is the uncorrupted image and F and η denote the bias field and noise, respectively. In the second model, the noise is scaled by the bias field:

$$I = (U + \eta)F. \tag{2.2}$$

The third model is, however, established upon *log* space transformation. In this notion, the logarithmic transformation of noise has one of the aforementioned distributions:

$$\log(I) = \log(U) + \log(F) + \eta. \tag{2.3}$$

These image models are occupied to iteratively correct the bias field by calculating U and F, alternately.

2.5.2. Partial Volume Effect (PVE)

Partial Volume Effect (PVE) refers to loss of contrast at the edges of two adjacent organs. The effect appears under two circumstances; (i) the first factor is due to lack of sufficient spatial resolution. The insufficient spatial resolution causes more than one tissue appearing in the same voxel; so, the resulting image is blurred. In other words, because of limited resolution, part of the signals from one object with stronger signals spill out into surrounding objects of weaker signals.

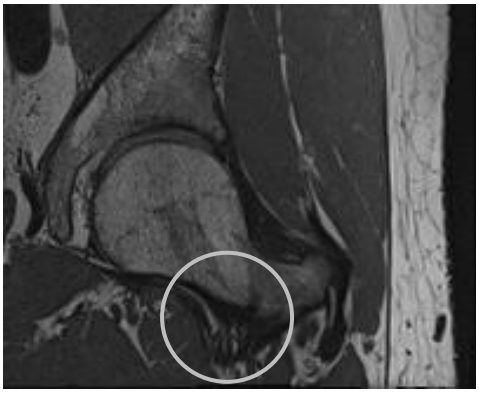

Figure 2.7. Partial Volume Effect resulting in blurred edges between fat and cortical bone and spongy bone and cortical bone and spill out effect due to insufficient resolution

(ii) The second factor of PVE is tissue fraction effect which refers to assignment of average intensity values to the voxels containing more than one tissue. Similar to first factor, the effect imposes spill out to the surrounding voxels.

PVE is considered to be an inevitable effect because of finite and discrete characteristic of image. Intuitively, it is impossible to map all points from the actual anatomical structure domain to discrete and finite range of image through a one-to-one function.

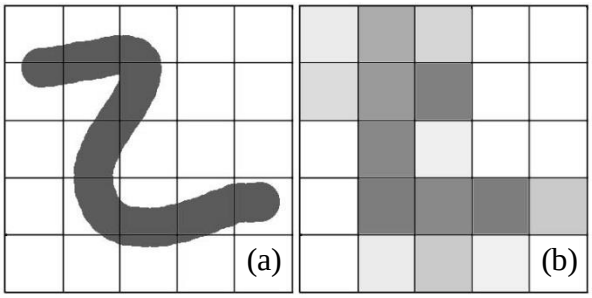

Figure 2.8. Tissue fraction effect (a) original object (b) spill-out effect

2.6. FAI Treatment

Two procedures of FAI treatment include non-surgical and surgical treatments; there are numerous non-surgical treatment methods of FAI consisting of medication, physical therapy, activity modification and steroid injection [9]. However, all of these methods are for temporary pain relief and cannot prevent the degeneration progression. Unlike non-surgical treatment, surgical treatment is considered as a permanent treatment of FAI aimed at removing the abnormalities in both pincer and cam types in order to avoid friction between femur and acetabulum. Actions performed during the FAI surgery contain [9]:

- *Osteoplasty* including rubbing the abnormal portion of femoral head-neck junction;
- *Reshaping* the acetabulum rim;
- *Removing* the cartilaginous dead tissues;
- *Debridement* or repair of labrum.

The challenge with surgical treatment is determining the direction of the intervention and the amount of bone to be removed to provide a painless motion for the patient. Hence, a preoperative system is required to assist in making flawless decisions [12].

CHAPTER 3

Image Segmentation Techniques in Magnetic Resonance Imaging

Myriad approaches for segmentation of medical images have been investigated so far. In this chapter, we focus on eight image segmentation categories that have been widely used in medical applications. We also describe the limitations of each methodology and the extensions to these procedures proposed to moderate the disadvantages associated with each approach. Our survey includes the following categories: thresholding, region growing, watersheds, clustering, graph-cut technique, atlas-based approach, neural networks and deformable models. Note that some experiments take advantage of more than one of these classes in order to compensate the deficiencies associated with the methodologies.

3.1. Thresholding

Thresholding is one of the basic techniques of image segmentation in which pixels located in one class lie within the same range of intensity defined by lower and upper thresholds. The base case of thresholding is binary or global thresholding that partitions image into two classes of foreground and background pixels with a single threshold; i.e.

$$L(p) = \begin{cases} 1 & I(p) \geq a_0 \\ 0 & I(p) < a_0 \end{cases} \tag{3.1}$$

where $L(.)$ is the threshold image and a_0 denote the threshold value which is often selected based on the image histogram.

A more general definition of thresholding considers more than two threshold values in order to divide the image into multiple regions of interest, a method called multi-thresholding and is formulated by

$$L(p) = \begin{cases} l_0 & I(p) \leq a_0 \\ l_1 & a_0 < I(p) \leq a_1 \\ & \vdots \\ l_n & a_{n-1} < I(p). \end{cases} \tag{3.2}$$

The method is suitable for the images with high inter-class contrast and coherent intra-class pixels i.e. it is most likely that the algorithm fails in presence of blurred edges, noise, variant illumination or other image artifacts. Additionally, selecting proper threshold values is often an awkward task and requires analysis of other image features. A solution was proposed by Otsu for automatic threshold selection [13]. Otsu is a non-parametric threshold technique in which intra-class variance is being minimized in order to find the optimized threshold values. In medical applications, Kalavathi used multiple Otsu thresholding for segmentation of white matter (WM), grey matter (GM), and cerebrospinal fluid (CSF) from MR images of brain [14]. The drawback with the author's approach is that in addition to computational time, the methodology is unable to address the issue with noisy or blurred images.

Thresholding performance can be improved by using local or adaptive thresholding. If the thresholds are selected with respect to statistical features in specified regions of the image, the method is called local. If constraints in (3.2) are set as functions of local properties of independent pixels or adaptive functions of spatial location, thresholding is called dynamic or adaptive [15, 16]. The methodology reveals acceptable results in segmentation of medical images [17, 18, 19]. Nevertheless, the process is computationally expensive and finding the appropriate function that works fine on all pixels is not always straightforward and the proposed functions are strictly application dependent.

3.2. Region growing

Region growing is a greedy approach to thresholding with locality feature distinguished by manually initializing a set of pixels as seed points inside the objects of interest. The process involves extending the set by checking homogeneity conditions on the neighbors of the pixels that are already members of the set; if the conditions hold the neighboring pixel is merged with the set. The thresholds adjust the connectivity and are determined according to prior knowledge in the application.

According to homogeneity criterion, four classes of region growing methods have been established [20]: Connected Threshold Region Growing, Confidence Connection Region Growing, Neighborhood Connected Region Growing and Isolated Connected Region Growing.

3.2.1. Connected Threshold Region Growing (CTRG)

CTRG is the simplest form of region growing in which thresholds are expressed explicitly; i.e. those pixels whose intensity is within an explicitly specified range, are added to ROI, iteratively.

3.2.2. Confidence Connection Region Growing (CCRG)

CCRG is based on dynamic calculation of mean and standard deviation of ROI using those pixels that are currently classified to be in ROI. Hence, the lower and upper thresholds are updated, iteratively:

$$lt = m - f\sigma$$
$$up = m + f\sigma \tag{3.3}$$

where m is the ROI mean, σ is the standart deviation and f is a user specified constant adjusting the effect of standard deviation.

3.2.3. Neighborhood Connected Region Growing (NCRG)

In NCRG, a shaped neighborhood is assessed for any pixel and the thresholding conditions are checked on the neighbors. If all the neighboring pixels lie within the threshold values then the underlying pixel is considered to be in ROI.

3.2.4. Isolated Connected Region Growing (ICRG)

The inputs of ICRG are a lower threshold and two seeds points that one of them is located in foreground and the other one is sampled from background. The algorithm uses binary search to find the proper upper threshold with respect to the seed points.

The approaches have been used in various medical imaging tasks. Mešanović et al. used histogram analysis for manual determination of thresholds in CTRG on CT images of lung [21]. Chang et al. utilized ICRG for colon segmentation [22]. Although proposed categories alleviate the thresholding restrictions associated with threshold selection, region growing suffers from the issues of over- or under- segmentation especially in presence of image artifacts. Due to the limitations, region growing is commonly applied as a preprocessing step or is combined with other algorithms. For example, Sivaperumal et al. incorporated CCRG with Pulse-Coupled Neural Network (PCNN) in order to automate the parameterization of PCNN [23]; in other

applications watershed and level sets were integrated with region growing in order to overcome the leakage problem [24, 25] . Furthermore, region growing was improved by occupying Genetic Algorithm (GA) for optimized selection of threshold values [26].

3.3. Watersheds

Watershed transformation is a region-based technique in which the image is represented as a topographic surface and segments are in correspondence with catchment basins separated by watershed lines. Catchment basin is defined as a set of points whose nearest local minima are identical. Watershed lines are also the functions for controlling flood level and are often a function of contrast or gradient.

The first step of the transformation is marker selection from which the topographic surface starts flooding. The marker selection is performed either manually or automatic [27, 28, 29].

Watershed algorithm has found many applications in medical image segmentation. Salman et al. used watershed for segmentation of tumors in CT and MR images of brain [30]. Mancas et al also proposed iterative watershed (IWS) for segmentation of spinous tumors in neck [31]. The significant disadvantages associated with watershed algorithm are sensitivity to noise and contrast, over-segmentation and inability in segmentation of thin structures [32]. Therefore, watershed algorithm is commonly hybridized with other methodologies or modified by prior knowledge [33, 34, 32, 35].

3.4. Clustering

Clustering algorithms are amongst the most popular techniques in medical image segmentation particularly for MR images [36, 37, 38, 39, 40, 41]. The approach refers to a family of unsupervised classifiers that partition the feature space into clusters [42]. Based on this expression, image segmentation can be viewed as a clustering task in which image regions are analogous to clusters. In MR images, the features are the properties such as T1-weighted, T2-weighted, proton and spin density values.

Thus far, numerous clustering algorithms have been introduced that commonly stem from one of the well-known algorithms namely *k*-mean (kM) and fuzzy *c*-means (FCM).

A renowned clustering algorithm that has been used for MR image segmentation is k-means [43, 44]. Expressing the algorithm in terms of image segmentation, a pixel belongs to one of the k segments of the image that has the nearest mean value to the intensity of the pixel. Thus, the following objective function is minimized within each segment:

$$F(S, M) = \sum_{j=1}^{k} \sum_{p_i \in S_j} \left\| p_i - \mu_j \right\|^2. \tag{3.4}$$

where μ_j is the mean of class j. In the approach, the assumption is that the segments are distinct i.e. the segmenting constraints are considered to be hard. On the other hand, FCM [45] is another approach that relaxes the constraint such that a pixel may belong to more than one segment assessed by a specific degree of membership. Comparatively, FCM gives better result for segmenting the overlapped data or obscure edges; nevertheless, since the procedure involves an optimization process, FCM appears to be time-consuming in its basic definition. For the aforementioned reason, many authors have target modifying the methodology for increasing the speed of the procedure. For instance, Al-Zoubi, et al., decreased the computational time by means of eliminating those points from distance calculation whose membership degree is less than a threshold value [46]. Li, et al. also proposed a modified FCM that used histogram information to optimize the number of iterations in segmentation of MR images [47].

A drawback of the classical FCM is that the calculations are only based on pixel intensity. Therefore, the performance of the method cannot be guaranteed in presence of noise or other image artifacts. To address this issue, Ahmed et al. presented FCM-S integrating spatial information in the objective function [36]. Subsequently, Li proffered FFCM-S, which speeds up FCM-S by modifying the membership degree [47]. Withal, the membership degree may not be calculated accurately in presence of noise; Krishnapuram et al. relaxed the normalized membership constraint, a new method they called possibilistic c-means (PCM) [48]. However, their method is sensitive to parameterization [49]. In addition to the referred extensions, there are numerous variations of FCM developed and applied in segmentation of MR images in order to resolve the issues with specific MR image artifacts. Some of the examples include modifying the cluster centers and membership degree [50, 51], estimating bias field [36, 52] and modifying the objective function [53, 54].

3.5. Graph-cut

Graph-based image segmentation provides a combinatorial optimization solution for image segmentation problem. The basic idea behind the approach is to convert an image into a graph such that every pixel corresponds to a vertex, the connection between two pixels is corresponding to an edge and the weight of the edge denotes the measure of similarity between the end pixels. Moreover, extra vertices *s* (source) and *t* (sink) are required to determine foreground and background labels. The edge set includes two types of edges; *n*-links that connect neighbouring pixels and *t*-links that connect the source and sink vertices to sample pixels marked as foreground and background, respectively. Considering the definition, image segmentation is equal to min-cut/max-flow problem on the established *s*-*t* graph for optimizing a second order MRF energy function:

$$E(L) = \sum_{p \in I} R(L_p) + \mu \sum_{p,q \in N} B(L_p, L_q) \tag{3.5}$$

where L is the set of labels, L_p denotes the label of pixel p, $R(.)$ is the penalty associated with assigning label L_p to pixel p and $B(.)$ indicates the penalty of assignment of two neighbouring pixels to distinct labels.

Min-cut/max-flow is a famed problem in theory of optimization and a variety of algorithms has been suggested in literature for solving the problem with different time complexities. Some of the strategies for most of the algorithms consist of push-relabel [55], augmenting path [56], linear programming [57] and Orlin's methods [58]. However, the algorithm that is frequently used in computer vision is based on the augmenting path technique by Boykov and Jolly [59]. In experiments with MR data, the approach was commonly used for segmentation of cardiac images [60] and brain images [61, 62]. Nonetheless, the method may fail in segmentation of the areas where edges are not sharp. Due to the failure, many publications incorporated a prior shape with the definition of the energy function. For example, Slabaugh et al. used an elliptical shape for segmentation of vessels and lymph nodes of pelvic MR images [63].Veksler employed a generic star shape for segmentation of convex structures by adding an additional shape term to the energy function [64]. Das et al. embodied the definition of compact shape into boundary term of the energy function and tested the approach for segmentation of eye balls from 2D MR image slices [65].On the other hand, Freedman and Zhang merged an arbitrary template with a graph-cut

based segmentation framework through illustrating a template as an unsigned distance function and modifying the energy function [66]; But, the assumption of their approach is that the prior shape is registered to the image. Grosgeorgea et al. suggested computation of PCA for modeling the shape variations and applied graph-cut segmentation technique with prior template manually registered on cardiac MR images [67].

3.6. Atlas-based Approaches

Atlas-based image segmentation is one of the useful segmentation approaches for cases where intensity information is insufficient. Atlas refer to statistical models of anatomy incorporating intensity properties and geometrical properties such as shape, orientation, continuity and smoothness that are reconstructed from a set of ground truth data. In this regard, Active Shape Models (ASM) [68] and Active Appearance Models (AAM) [69] can be considered as atlases [70]. Therefore, the model can facilitates the delineation of test images by provision of prior knowledge about the region of interest.

Atlas-based segmentation involves two critical steps; the first step is atlas construction and various the techniques have been proposed so far [71, 72, 73, 74]. At the second step, however, the accuracy of the solution for segmentation problem relies on an image registration technique. A comprehensive survey about image registration techniques is covered in [75]. There are three common components in any image registration algorithms:

- *Transformation* from one space to the space of reference including rigid and non-rigid transformations;
- *Objective function* to evaluates the measure of similarity between the two datasets;
- *Optimization method* to advance the objective function.

Several papers have been published for any of the aforementioned concepts over years contributing to various classes of image registration techniques [76, 77]. In segmentation of MR images, atlas- based methodologies have been widely applied for delineation of brain [78, 79, 80], cardiac [81, 82] and breast data [83, 84].

While a large number of atlas-based techniques are available, a limited number of them are practically suitable for clinical studies. This is because handling all variations of anatomy by deforming a limited set of models is a complicated task; i.e. the atlas model may not be enough

for modelling all statistical variations of the anatomy. Furthermore, atlas-based approaches often miss local image features for registering the atlas model to the image [85].

3.7. Neural Networks

Artificial Neural Networks (ANNs) are simplified computational models inspired by properties of biological nervous systems. The algorithms have been developed for solving a variety of problems inclusive of image segmentation. Data analysis via neural networks is often performed by three strategies. The first category of algorithms involve supervised procedures that use a set of training data to adjust the parameters of the network i.e. the network is learned against ground truth data and can appraise the output for a set of test data by applying the learned parameters on input data. A challenge of this approach is evaluation of the network in terms of trained parameters. To put it another way, the trained system should be examined in order to insure that it has not been under- or over- trained. To avoid the problem numerous techniques have been suggested [86, 87, 88, 89]. The second strategy is an unsupervised mechanism that works with a set of unlabeled training data to tune the parameters of the network from individual patterns. The third scenario involves semi-supervised learning that takes advantage of labeled and unlabeled data. The scheme is useful particularly for the situations where labeling the whole training set is either time-consuming or requires expertise [90].

Variations of ANNs have been used for medical image segmentation. Indeed, the most popular algorithm applied to diverse problems is Self-Organizing Map (SOM) [91]. The network relies on an unsupervised learning module to transform the input data with arbitrary dimensions to one or two-dimensional topographic map; expressly, a lattice of neurons is formed so that the relative position of the nodes is tuned according to the input features. The network has been extensively used for segmentation and reconstruction of 3D anatomy specifically cerebrum in MR images [92, 93, 94, 95]. Albeit, the examples of using neural networks in segmentation of joints are very rare, few researchers have tried to apply neural networks for segmentation of bones [96, 97] and cartilage [98].

3.8. Deformable models

Categorically, the most popular and accurate algorithms for medical image segmentation for both research and clinical purposes belong to the family of deformable models. Two main classes of deformable models are parametric [99, 100] vs. geometric models [101, 102]. A thorough survey of parametric deformable models is available in [103]. In addition, a comprehensive review of methods of geometric models is covered in [104]. The idea of both algorithms is evolution of a dynamic model; however, their difference is in the formulation of the problem. Specifically, the parametric models are parameterized explicitly opposing to geometric models with implicit representation.

The model in geometric representation (also called level set approach) has an implicit parameterization. The model is represented by a zero level set function of time i.e. $\phi(x(t), t) = 0$ and the evolution equation is

$$\phi_t + F|\nabla\phi| = 0 \tag{3.6}$$

where F denotes the speed function defined for controlling the motion of the front. The shortcomings of basic level set are difficulty for constructing the speed function as well as costly computation. However, several level set segmentation techniques suggest solutions for the issues.

The variations of level set techniques have been broadly employed for segmentation of MR images of brain [105, 106, 107, 108], cardiac data [109, 110, 111] and liver [112, 113].

However, parametric deformable models are preferred to geometric models in segmentation of higher dimension objects since they can provide a means for coherent inter-slice segmentation. Theoretically, the goal of parametric model image segmentation is minimization of a Lagrangian energy function. Let *M(s)* be a parametric model, then:

$$E(M) = \int E_{int}(M(s)) + \int E_{ext}(M(s)) \tag{3.7}$$

Popular parametric deformable contour algorithm better known as “snakes” [99] is a special case of multi-dimensional parametric deformable models (PDM). The evolution is based on theory of deformable models that is derived from theory of elasticity in physics targeting dynamics of computer graphics objects. Unlike most classical computer graphics modeling techniques, models are regarded to be active rather than passive; i.e. on top of simulation of

kinematics of the object, the physics of the model are taken into consideration including the influential forces or energies from the enclosing environment [114].

As suggested by the theory, PDMs are sufficiently versatile to adapt to any environment depending on the representation of the environment to the system in terms of energies or forces. The characteristic has caused many researches to target deformable models in a variety of segmentation tasks each of which is accompanied by a specific improvement in order to overcome the limitations imposed by classic definition of models [115, 116, 117, 118, 119, 120, 121].

A desirable feature of PDMs is their scalability to higher dimensions. Primitively, Terzopoulos et al. simulated dynamics of deformable surfaces [114]. Subsequently, several enhancements have been made that originate from the stated idea. Delingette et al. represented the object as a free-form deformable surface [122]. Also Cohen et al. applied deformable surfaces for segmentation, visualization, and tracking the organs [123]. In another work, they used a balloon model for a surface described as an aggregation of contours [124]. In order to handle the topological changes McInerney et al. suggested an affine cell image decomposition to formulate the surfaces by an automatic reparameterization [125, 126]. Other efforts majorly are focused on involving supplementary measures such as shape similarity, intensity, etc. For example, Alfiansyah et al. incorporated local intensity variation for segmentation of ultrasound images [127].

Although PDMs take advantage of local features, a distinguished limitation of them is associated with weak effect of gradient forces in plain areas of the underlying image where the gradient magnitude is approximately zero. This may lead to domination of internal forces to external forces inducing under-segmentation problem. To resolve the issue Cohen introduced balloon force that is a constant force to enable inflation of the object surface making the model passes over the spurious edges and plain areas [128]. However, in Cohen's approach, the balloon force is non-parametric and the model expands autonomously which causes over-segmentation at some points. Our approach uses a similar idea for expanding the model on selected points; i.e. the model expands at the points satisfying particular constraints.

Another restriction of deformable models is that obtaining a good performance necessitates locating the initial model sufficiently close to boundaries of ROI. Front initialization task is

divided into three general categories: manual, semi-automatic and automatic initialization [129]. In manual initialization the location of all points are determined by the user; as opposed to manual initialization, automatic initialization does not involve any human interaction. Compared to automatic method, semi-automatic initialization refers to partial human interaction in relocating a subset of points and allowing the rest of the points to be assigned automatically. An example of automatic model initialization based on mathematical morphology and thresholding is proffered by Rahnamayan, et al. for automatic initialization; however, their method works well only for images with homogeneous areas [130]. Thus, the most reliable approach is to use a semi-automatic algorithm to make sure that the model is located close enough to ROI boundaries and is closely related to our technique.

CHAPTER 4

Methodology

The outline of our methodology is described as follows: in the preprocessing step, our objective is to reduce the noise and pseudo-edges by means of enhancing and smoothing; so that the major edges are preserved and the redundant edges that show up in the form of minor artifacts disappear by the smoothing filter. At the same time, an atlas mesh model is deformed on the image by sampling points from the model and assessing the corresponding landmarks from the image. PDMs turn out to have better performance in the regions with spurious edges in comparison with other techniques due to elasticity and evolution based on local features. Nevertheless, as stated earlier, the accuracy of the method can be influenced by initialization of the model; especially, it is most likely that the model is trapped in local false edges during evolution. To pass over these traps one way is to place the initial model close enough to the boundaries of ROI. To this aim, we proposed a semi-automatic initialization that can benefit from the knowledge that is provided by the user particularly in the areas where the model is likely to stray. The 3D PDM framework in the second phase is specifically capable of skipping the minor traps by means of a thresholded balloon force.

The pipeline of the approach is shown in Figure 4.1. As illustrated, the inputs of the schema are a set of MR images and an atlas mesh model. The input model is a triangular mesh with predefined connections that are preserved during the evolution. After the images are preprocessed, the landmark points from the image and their corresponding control points from the mesh model are selected to be used in the registration process. After this step, the model is initialized on the image and supposed to segment the ROI to a coarse level i.e. the model should be located close to the boundaries of ROI provided that the selections are performed properly. Hereby, a PDM method is applied for a coarse-to-fine level segmentation.

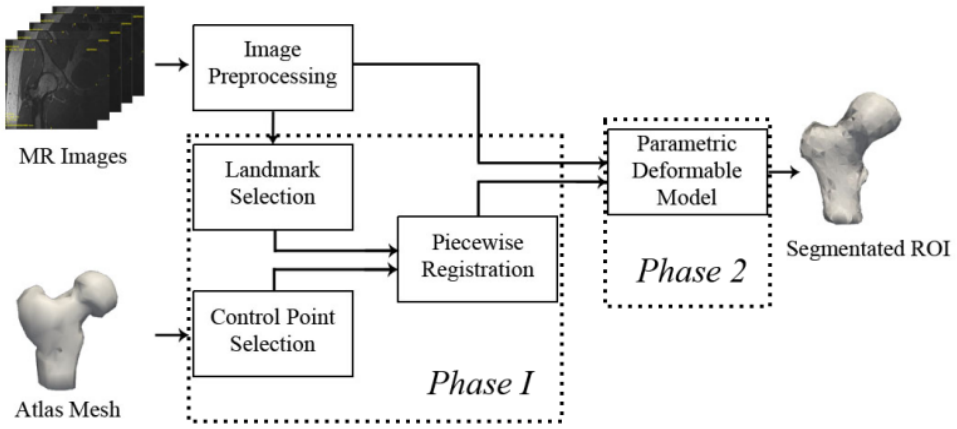

Figure 4.1. Overview of the proposed approach

4.1. Image Preprocessing

Image preprocessing involves histogram equalization for edge information enhancement followed by a gradient minimization smoothing filter using L0 information. In this section, we discuss the theory of each step in great detail.

4.1.1. Enhancing Histogram Equalization

Histogram equalization is amongst basic algorithms of image enhancement. Let $I(x,y)$ be an image with pixel intensity levels $0,\dots,L-1$ and $h(I)=\{p_i|i=0,\dots,L-1\ ,\ 0\le p_i\le 1\ ,\sum_i p_i=1\}$ denote the normalized histogram of the image. Then the histogram-equalized image is defined as

$$I'(x,y)=T(k)\quad s.t.\quad I(x,y)\ \epsilon\ level\ k,$$
$$T(k)=(L-1)\sum_{i=0}^{k}p_i. \tag{4.1}$$

An advantage of the algorithm is that it is not computationally expensive which is particularly

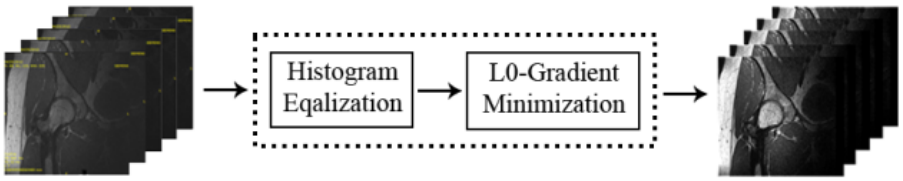

Figure 4.2. Image Preprocessing

desirable in medical applications.

4.1.2. Smoothing MRI data using L0-Gradient Minimization

The image smoothing filter uses the definition of L0-norm of gradient and was proposed by Xu et al. [131]. The algorithm is particularly suggested for preserving the major edges and ignoring the minor details e.g. noise by means of reducing the number of local intensity variations. As a result, the output is a piecewise image constituting relatively unvarying regions that are useful in region-based processing. In some sense, the method can be considered as a segmentation procedure as long as the ROI does not include significant intensity variations. However, in our case the method does not suffice because of the inherent inhomogeneity of the bone data.

Expressly, let $I(x,y)$ be an image and $S(x,y)$ denote the corresponding smooth image. We define set G of image coordinates as follows:

$$G = \{\,(i,j) \mid \left|\frac{\partial S(i,j)}{\partial x}\right| + \left|\frac{\partial S(i,j)}{\partial y}\right| \neq 0\,\}. \tag{4.2}$$

According to (4.2), L0-norm of gradient of $S(x,y)$ is determined by the number of elements in G; i.e.

$$C(S) = card(G). \tag{4.3}$$

Intuitively, a feasible solution for S is obtained by solving an optimization problem that maximizes the similarity measure between input and output images and minimizes the number of edges; the similarity measure is formed by sum of squared intensity difference. Given these facts, $S(x,y)$ is estimated by minimizing the objective function

$$f(S) = \sum_{i,j}(S(i,j) - I(i,j))^2 + \rho C(S) \tag{4.4}$$

where ρ is the smoothness coefficient controlling the effect of $C(S)$. For minimizing the objective function in (4.4), an estimating function is defined that introduces two auxiliary variable corresponding to the gradient in x and y direction. Thus, the new objective function is a three variable function expressed as

$$f'(S,\alpha,\beta) = \sum_{i,j}(S(i,j) - I(i,j))^2 + \rho C(\alpha,\beta) + \mu((\frac{\partial S(i,j)}{\partial x} - \alpha(i,j))^2 + (\frac{\partial S(i,j)}{\partial y} - \beta(i,j))^2) \tag{4.5}$$

procedure S=L0_Gradient_Minimization $(I, \rho, \mu, \mu_{max}, \mu_{rate})$
  initialize $S \leftarrow I$
  do
    obtain $\big(\alpha(i,j), \beta(i,j)\big)$ by solving (4.7);
    obtain S by solving (4.6);
    $\mu \leftarrow \mu_{rate} * \mu$
  while $(\mu \leq \mu_{max})$
end

Algorithm 4.1. . L0-Gradient Minimization smoothing filter

The optimized solution with objective function $f'(.)$ is obtained by letting

$$S = F^{-1}\{\frac{F(I) + \mu(F(\partial x)^* F(\alpha) + F(\partial y)^* F(\beta))}{F(1) + \mu(F(\partial x)^* F(\partial x) + F(\partial y)^* F(\partial y))}\}, \tag{4.7}$$

and

$$\big(\alpha(i,j), \beta(i,j)\big) = \begin{cases} (0,0), & \left(\frac{\partial S(i,j)}{\partial x}\right)^2 + \left(\frac{\partial S(i,j)}{\partial y}\right)^2 < \frac{\rho}{\mu} \\ \left(\frac{\partial S(i,j)}{\partial x}, \frac{\partial S(i,j)}{\partial y}\right), & otherwise \end{cases} \tag{4.8}$$

where $F(.)$ denotes the Fast Fourier Transform (FFT) and * is the complex conjugacy. Also, $F(1)$ indicates the FFT of Dirac delta function. The steps of the algorithm are shown in Algorithm 4.2.

We have represented the result of applying the filter on two images (Figure 4.3). The methodology show promising results in removing salt and pepper noise (Figure 4.3(a)) and the natural non-uniformities of the anatomy (Figure 4.3(c)). The piecewise image is highly useful in segmenting ROI by means of region-based terms. Allegedly, due to existence of constant regions, establishing a deformable model framework only based on edge information may cause failure in the segmentation process of the smooth image. In other words, elimination of minor gradient information that are often considered as disturbing factors, causes domination of internal forces and shrinks the models.

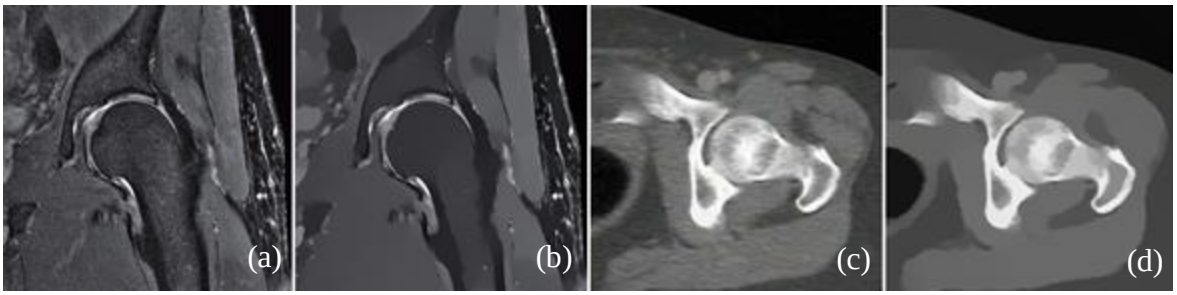

Figure 4.3. L0-Gradient Minimization (a) original noisy image (b) L0-gradient minimized image with $\boldsymbol{\rho} = \mathbf{0.01}$, $\mu_{rate} = \mathbf{10}$, $\mu = \mathbf{0.02}$, $\mu_{max} = \mathbf{10^5}$. **(c) MR image of knee joint (d) L0-gradient minimized image with** $\boldsymbol{\rho} = \mathbf{0.015}$, $\mu_{rate} = \mathbf{20}$, $\mu = \mathbf{0.03}$, $\mu_{max} = \mathbf{10^5}$.

4.2. Initialization

As declared earlier, PDMs are most likely to get trapped in local false edges during evolution. To skip these traps one way is to place the initial model close enough to the boundaries of ROI. Manual initialization is both time-consuming and cumbersome specifically for mesh models with high complexity. The issue lends weight to need for either a semi-automatic or automatic mesh initialization. However, a major problem with automatic approach is the lack of guarantee for correct front placement. A reliable approach is to use a semi-automatic mesh initialization. In this work, we use a semi-automatic technique that utilizes a Radial Basis Function (RBF) interpolation for initializing a mesh model with high complexity by determination of a few numbers of vertices on the edges of ROI. To rephrase, having a model of the anatomy, RBF interpolation acts as a piecewise registration procedure to establish a coarse model close to the boundaries of ROI.

4.2.1. RBF Interpolation

Radial basis function interpolation is proposed to estimate the new positions for a set of desired data points using sample points with known positions also known as control points. The methodology has been widely used in the area of computer graphics and animation for mesh morphing.

Let $f(.)$ be a displacement function $\mathbb{R}^3 \rightarrow \mathbb{R}^3$ whose value is known at control points; thus, for control point $c_i = (x_i, y_i, z_i)$

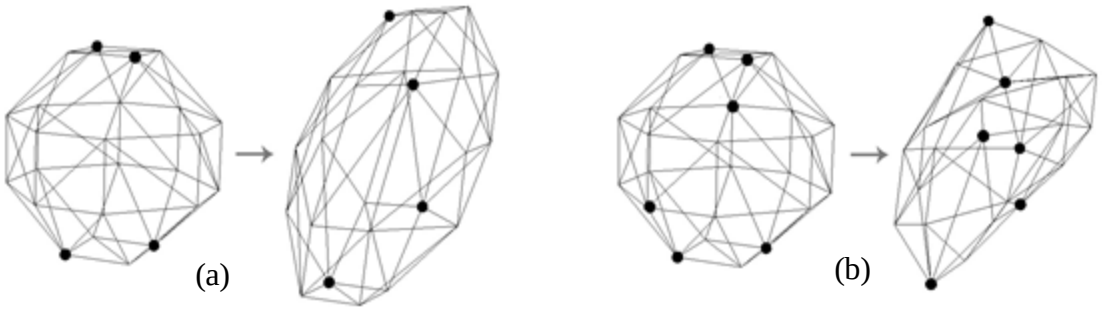

Figure 4.4. Radial Basis Function Deformation (a) object deformed by 4 control points using a Multi-quadric kernel function (b) object deformed by 6 control points using a Multi-quadric kernel function

$$f(c_i) = \gamma_{i\,,} \quad i = 1, \dots, N \tag{4.9}$$

where N is the total number of control points ; for unknown values, displacement function is expressed as follows:

$$\begin{gathered} f(x) = \sum_{i=1}^{N} \lambda_i \phi(\|x - c_i\|) + p(x), \\ p(x) = \mu_0 + \mu_1 x + \mu_2 y + \mu_3 z \end{gathered} \tag{4.10}$$

where $\phi(.)$ is a radial basis function and λ_i and μ_i are RBF and polynomial coefficients, respectively. Additionally, the set of following conditions must hold:

$$\sum_{i=1}^{N} \lambda_i q(c_i) = 0. \tag{4.11}$$

where $q(.)$ denotes any polynomial with a degree less than or equal to $p(.)$. To determine the unknown values λ_i and μ_i the following system is to be solved

$$\begin{bmatrix} V & P \\ P^T & 0 \end{bmatrix} \begin{bmatrix} \Lambda \\ B \end{bmatrix} = \begin{bmatrix} \Gamma \\ 0 \end{bmatrix}, \tag{4.12}$$

where

$$\begin{gathered} V = \left[\phi\left(\|c_j - c_i\|\right)\right]_{N \times N}, \\ P = [1\ x_i\ y_i\ z_i]_{N \times 4}\,, \\ \Lambda = [\lambda_i]_{1 \times N}, \\ B = [\mu_i]_{1 \times 4}. \end{gathered} \tag{4.13}$$

Hence, the new position for data points is obtained by

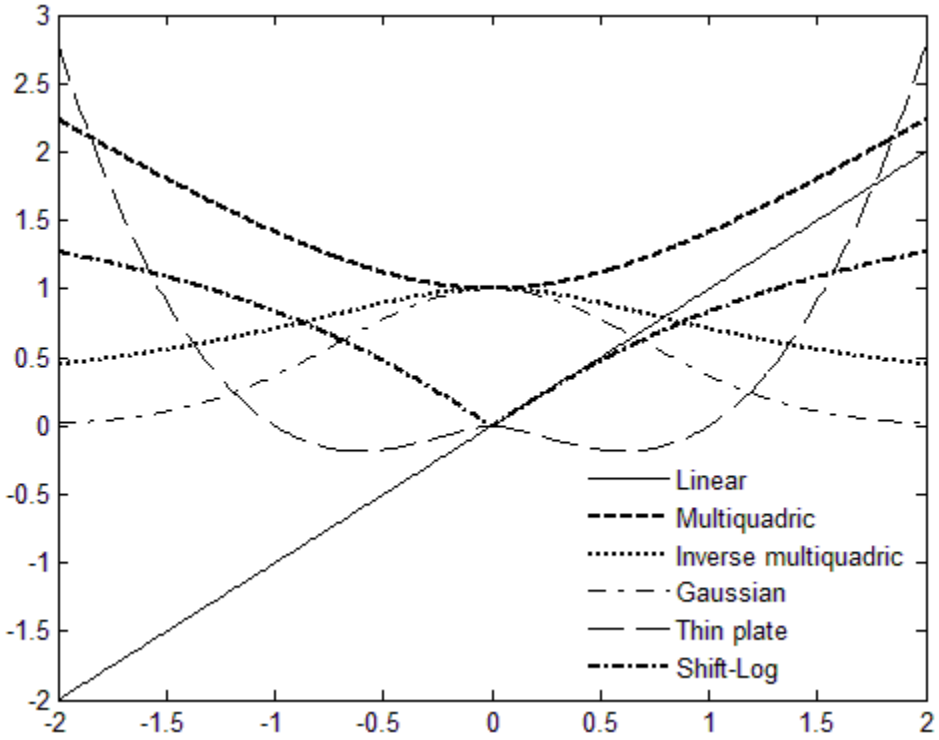

Figure 4.5. Radial basis functions ($\boldsymbol{\varepsilon} = \mathbf{1}$)

$$x' = x + f(x). \tag{4.14}$$

There are numerous radial basis functions referenced in literature. Some of the frequently used types of functions are listed in the table below:

Function name	Functional equation
Linear	$\phi(r) = r$
Multiquadric	$\phi(r) = \sqrt{1 + (r\varepsilon)^2}$
Inverse multiquadric	$\phi(r) = 1/\sqrt{1 + (r\varepsilon)^2}$
Gaussian	$\phi(r) = \exp(-(r\varepsilon)^2)$
Thin plate	$\phi(r) = r^2 \ln(r)$
Shifted-Log	$\phi(r) = \sqrt{\ln(r^2 + \varepsilon^2)}$

Table 4.1. Radial basis functions ($\boldsymbol{\varepsilon}$ is a constant)

4.2.2. RBF Interpolation for Model-to-Image Piecewise Registration

An advantage of radial basis functions is that the method is consistent with scattered data and the deformation is based on a point-by-point scheme; expressly, unlike an elastic system, neighbourhood connectivity has no role in deformation. This property is highly desirable in medical applications since anatomical models have custom shapes. Strictly speaking, the shape of

the anatomy varies with respect to patient and time and modeling an anatomy as a structured mesh model may lead to poor results. On the other hand, unstructured grids provide enough flexibility to adapt the initial models to personalized data and RBF interpolation can be an excellent match for deformation of this type of mesh models.

In our application, RBF deformation is regarded as a piecewise registration method. In other words, given an atlas model, the model is semi-automatically initialized on the ROI by a piecewise registration routine. The input of the routine is an atlas mesh model and a subset of vertices (v_i) as control points and their corresponding landmarks (l_i) from the image. So, the displacement function in (4.8) is rewritten as

$$f(v_i) = l_i - v_i, \quad i = 1, \dots, N \tag{4.15}$$

Finally, the new position of the rest of the atlas vertices are calculated by (4.13) and the model is registered to the image.

4.3. Parametric Deformable Model (PDM)

After applying RBF piecewise registration, the ROI in the image is coarsely segmented. As mentioned, the assumption for piecewise registration is to consider the model in a point-by-point scheme; however, in a parametric deformable model framework the model is supposed to be elastic. So, for coarse-to-fine segmentation we assume that the model is transformed from a point-by-point scheme to an elastic scheme.

Parametric deformable models (PDMs) are discrete elastic objects defined by a set of nodes and their connectivity with neighboring nodes; in this sense, the object is represented explicitly. There are two approaches for formulating the evolution of PDMs. The formulation is a greedy algorithm that utilizes the principle of energy minimization. However, the second one is a dynamical approach that conceptualizes the evolution of the model in terms of effective physical forces. Although both formulations contribute to the same results, the physics-based approach is especially preferred in problems of higher dimensions due to provision of a more flexible scheme. In the following sections, we discuss the functionality of each approach briefly.

4.3.1. PDM Greedy Approach

The greedy algorithm is an energy minimizing approach and an effort for global minimization supposedly occurring at the edge of the ROI. In thermodynamics point of view, the model at the edges of ROI is supposed to be a thermodynamic equilibrium system where the sum of internal and external energies is zero.

The formulation is a discrete representation of (3.7) so that the energy is calculated at each vertex of the model and the energy of the whole model is determined by the sum of absolute value of the energy at each vertex. The energy at each vertex is the sum of two opposing energies; i.e.

$$E(p_i) = E_{int}(p_i) + E_{ext}(p_i) \quad i = 1, \dots, M \tag{4.16}$$

The first type of energy is internal energy reflecting local properties of the model. Internal energy is obtained by weighted sum of two commonly used energies i.e. tension and smoothing energies that exploit distribution of the vertices and rigidity of the model, respectively. Both energies take advantage of geometrical properties of the model and have no linkage to the image. On the other hand, local image properties are examined through external energies. One common type of external energy is based on image boundary information at the neighbourhood of the pixel/voxel containing the vertex. However, the framework is sufficiently flexible to be customized for optimization of other image or model properties.

4.3.2. PDM Dynamic Approach

Physics-based approach simulates the evolution of the model as a dynamic problem. The goal of the algorithm is to reach a state where the sum of acting forces is zero and the model has no motion. The approach is considered as a vector representation of the energy-based approach and the displacement of the vertices over time follows Newton's law of motion

$$\vec{F}(v_i) = m\frac{d^2 v_i}{dt^2} + \eta\frac{dv_i}{dt} \quad i = 1, \dots, M \tag{4.17}$$

where M is the number of all vertices, m is the object mass and η is the viscosity coefficient. For simplicity, m is often set to zero; thus, the effect of acceleration is excluded and the evolution is accomplished at a constant velocity. Using Euler method and 4.16, the new position for i-th vertex is obtained by

$$v_i^{t+1} = \overrightarrow{F'}(v_i^t)\Delta t + v_i^t \quad i = 1, \dots, M \tag{4.18}$$

where $\overrightarrow{F'}(v_i^t) = \frac{1}{\eta}\vec{F}(v_i^t)$. $\overrightarrow{F'}(.)$ is expressed as the sum of internal and external forces,

$$\overrightarrow{F'}(v_i^t) = \overrightarrow{F_{int}}(v_i^t) + \overrightarrow{F_{ext}}(v_i^t) \quad i = 1, \dots, M. \tag{4.19}$$

Similar to energy-based approach the forces are results of summation of predefined normalized forces whose effectiveness coefficients are adjusted by the user. In this work, we have customized the forces in order to overcome the deficiencies associated with classical deformable model forces.

4.3.2.1 Internal Forces

We consider two types of internal forces to control the distribution of mesh points over the surface of the object as well as the smoothness of the mesh to avoid mesh non-rigidities and complications.

4.3.2.2 Tension Force

Tension force adjusts the effect of neighboring vertices on the evolution of a vertex by regularizing the distance between them; thereupon, the vertices are distributed evenly on the surface of the model. The force is expressed as

$$\overrightarrow{F_T}(v_i) = \sum_{x_j \in N(x_i)} (h - \|x_j - x_i\|) \frac{(x_j - x_i)}{\|x_j - x_i\|}, \quad i = 1, \dots, M. \tag{4.20}$$

In this equation, h denotes the global mean distance between any two neighbouring vertices:

$$h = \sqrt{\frac{1}{M}\sum_{i=1}^{M}\left(\frac{1}{card(N(x_i))}\sum_{x_j \in N(x_i)}(x_j - x_i)\right)} \tag{4.21}$$

4.3.2.3 Laplacian Smoothing Force

Numerous techniques of mesh smoothing are proposed in various publications. One of the most popular algorithms is Laplacian smoothing that we applied as an internal force in order to bind the vertices on a smooth surface and conserve the rigidity. The expression of the force is

$$\overrightarrow{F_S}(v_i) = \frac{1}{|N(x_i)|} \sum_{x_j \in N(x_i)} x_j - x_i \quad i = 1, \dots, M \tag{4.22}$$

Apparently, the force pushes the vertices towards the centroid of the area formed by their neighbours.

4.3.3. External Forces

In classical PDM the external force constitutes the gradient force that is related to spatial derivation of gradient image; i.e.

$$\overrightarrow{F_{Grad}}(v_i) = -\nabla \|\nabla I(v_i)\| \tag{4.23}$$

where $I(v_i)$ denotes the image coordinate of the pixel/voxel that includes v_i. There are two immediate drawbacks with this definition: (i) the magnitude of $\overrightarrow{F_{Grad}}$ is affected by the intensity of the pixels/voxels in gradient image and this may lead to fluctuations or surging at the model vertices; (ii) the magnitude of the force is insignificant in plain areas of the image causing domination of internal forces to external forces and model shrinkage. To address these issues we have introduced two custom external forces instead of classical definition which are discussed in the following sections.

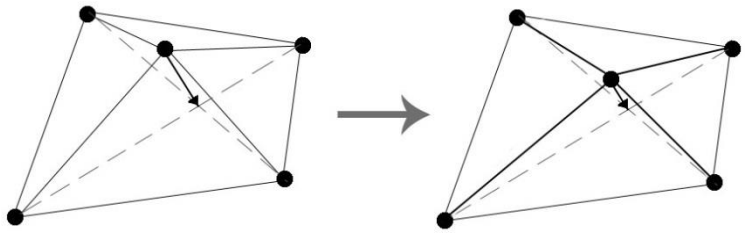

Figure 4.6. Laplacian Smoothing

4.3.3.1 Delingette's Gradient Force

The force was proposed by Delingette to establish a position-based force rather than an intensity-based force in order to compensate for the first issue [132]. The profound feature of this approach is that the vertices do not fluctuate by the rate of changes in the intensity of gradient image. The force is obtained by projection of vector $\overrightarrow{t_i}$ on the normal vector and is expressed by

$$\overrightarrow{F_D}(v_i) = \left(\overrightarrow{t_i}.\overrightarrow{n_i}\right)\overrightarrow{n_i} \quad i = 1, \dots, M. \tag{4.24}$$

where $\overrightarrow{n_i}$ is the i-th vertex normal vector and $\overrightarrow{t_i}$ is a translation vector of v_i that repositions vertex v_i to the voxel with the local maximum intensity of gradient image in a $k \times k \times k$ neighborhood. Note that the translation is calculated in image domain and the result is transformed to physical domain with respect to voxel spacing.

4.3.3.2 Thresholded Balloon Force

The force is similar to balloon force with the difference that it uses upper and lower threshold values to constraints the displacement of the vertex; i.e.

$$\overrightarrow{F_B}(v_i) = \begin{cases} \overrightarrow{n_i}, & a \leq \mathcal{I}(n_{v_i}) \leq b \\ \vec{0}, & otherwise \end{cases} \tag{4.25}$$
$$i = 1, \dots, M$$

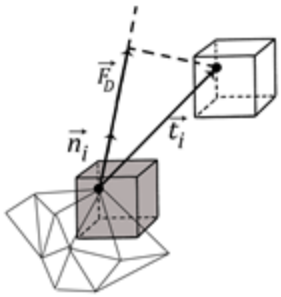

Figure 4.7. Delingette's gradient force

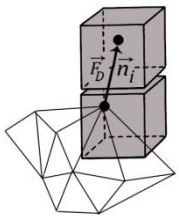

Figure 4.8. Balloon force

where a and b are lower and upper thresholds, respectively; additionally, $\mathcal{I}(n_{v_i})$ refer to the intensity of the voxel appearing in the direction of the normal of vertex v_i.

Having all the forces, for any type of force a coefficient exists that control the effect of the acting force in the motion of the model; rewriting (4.18), we have

$$\overrightarrow{F'}(v_i^t) = \alpha\overrightarrow{F_T}(v_i) + \beta\overrightarrow{F_S}(v_i) + \gamma\overrightarrow{F_D}(v_i) + \delta\overrightarrow{F_B}(v_i) \tag{4.26}$$

We explained the fundamentals of the two approaches. However, comparing two approaches, greedy algorithm has to be accompanied by an extra step after visiting all vertices. The step is called remeshing and is performed in order to avoid overlap. The idea is that considering two windows of width l centred at neighbouring pixels/voxels, if the two windows overlap at time t the vertices are likely to overlap at time $t+1$. Therefore, the distance between the two pixels at any dimension has to satisfy the following constraint:

$$l \leq \left\| p_i - p_j \right\|_\infty \leq 2l \tag{4.27}$$

Consequently, the complexity of greedy algorithm is $O(ln)$ while there is not such a procedure in dynamic approach and the time complexity is $O(n)$ [133].

CHAPTER 5

Evaluation, Results and Validation

In this chapter, we explain the details of the evaluation process for comparing the obtained results with ground truth(GT) data; and, we present the results of our segmentation framework on a synthetic dataset and two sets of clinical MR images of hip. Eventually, we compare our results with other PDM methods.

5.1. Evaluation

5.1.1. Data Conversion

As illustrated, the output of the scheme is a smooth mesh model. Since, the mesh model is defined in continuous physical space rather than discrete image space, for evaluation of segmentation we have to transform the model into image space i.e. we need to convert mesh model to discrete image data.

One way for converting the polygonal data to image data is generating an image stencil from the polygon. The input for the process is the mesh and size of the desired image and the output is

```
procedure I=MeshToImage (image_size, mesh)
    initialize I ← white_image(image_size);
    cut mesh at each z-slice of I;
    for each slice z of the mesh
        if there exist loose ends connect them by a line;
        for each line segment i in slice z
            for each integer value y in line segment j
                store (x,y,z) in matrix M where value x is an integer value at that point
            end
        end
    end
    I=cookie-cut I with stored coordinates to create a binary image;
end
```

Algorithm 5.1. Mesh to image conversion algorithm

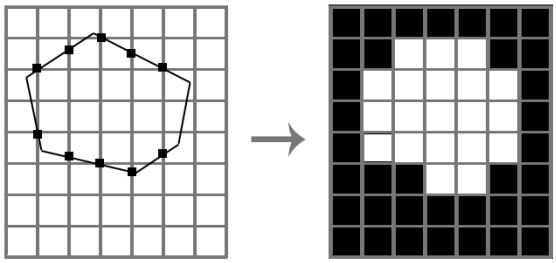

Figure 5.1. 2D polygon to image conversion

a binary image for which the intensity of the voxels inside the polygon is 1. The details of the conversion algorithm are shown in Algorithm 5.1.

5.1.2. Evaluation Metrics

After obtaining the image from the mesh data, the next step is to compare the results with ground truth (GT) segmented image which is also represented by a binary image. The performance is then quantified by the following statistical overlapping measures:

$$TO = \frac{TP}{TP + FN}$$
$$Er = \frac{1}{2}\left(\frac{FP}{TP + FP} + \frac{FN}{TP + FN}\right) \tag{5.1}$$

where TO and Er denote target/GT overlap and misclassification error, correspondingly. Additionally, TP, FP and FN are cardinality of true positive, false positive and false negative sets of voxels, respectively. All measures are normalized values in the range [0, 1] describing the ratio of correct segmentation in comparison with the GT data.

With the aforementioned measures, to evaluate the accuracy of the method the metrics have to be compared in correspondence; for instance, an increase in TO is not necessarily interpreted as a better segmentation. In this case a better performance is achieved if TO increases while Er is reduced. In other words, considering TO as an individual measure may lead to misinterpretation about the accuracy of the method.

Regarding the evaluation strategy, we present the results of applying our method on synthetic and clinical MR data.

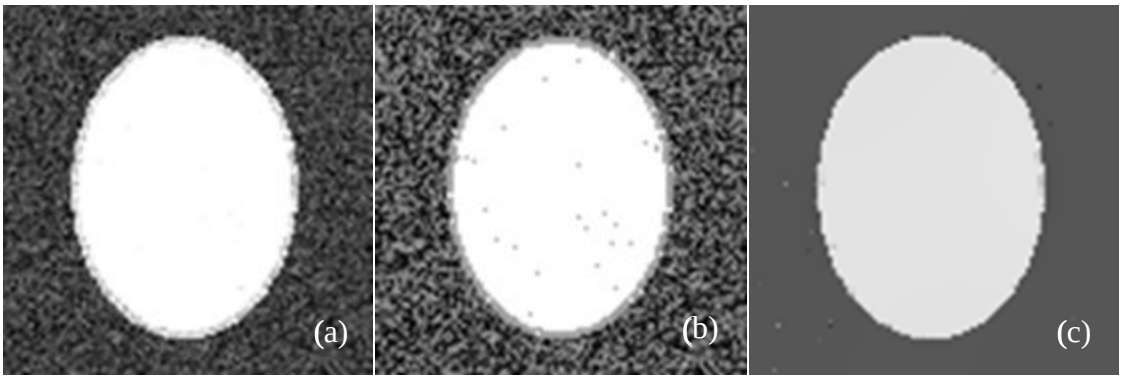

Figure 5.2. Sample slice from synthetic data (a) original image (b) histogram equalized image ($\boldsymbol{nbin = 64}$) (c) L0-smooth image ($\boldsymbol{\rho = 0.03}$, $\mu_{rate} = \mathbf{2.0}$, $\mu = \mathbf{0.06}$, $\mu_{max} = \mathbf{10^5}$)

5.2. Results

5.2.1. Segmentation of Synthetic Image Data

The synthetic image sequence consists of 100 greyscale images of size 100×100 pixels corrupted by Gaussian noise of σ=0.25. The proposed ROI is an ellipsoid with dark and thick borders generated manually on each slice by the following equation

$$(\frac{x-50}{40})^2 + (\frac{y-50}{30})^2 + (\frac{z-50}{20})^2 \leq 1 \qquad (5.2)$$

GT data is generated simultaneously and represented as a binary image.

5.2.1.1 Image Preprocessing

The result of applying the preprocessing block is shown in Figure 5.2. As can be seen the details including noise and edges have been enhanced by histogram equalization. However, the smoothing filter has alleviated the noise while preserving the edges of ROI. Hence, the output of the filter is a piecewise image.

The result can be also concluded from statistical analysis of the whole dataset (Figure 5.3). Considering the final histogram of the 3D data before and after preprocessing block with the same parameter setting on all slices, the major range of intensity of foreground and background areas of the image can be easily observed; i.e. the intensity of foreground voxels is between *[0.8, 0.9]* and intensity of majority of background voxels is in interval *[0.3, 0.5]*. The information can be especially useful for selecting the threshold values in thresholded balloon force. Note that

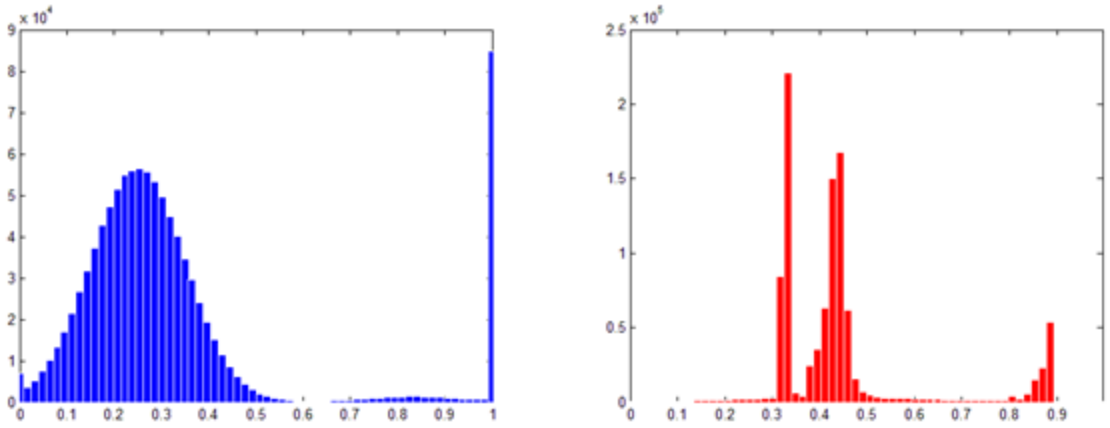

(a) (b)

Figure 5.3. Histogram of 3D synthetic data (a) original 3D volume (b) after preprocessing ($\boldsymbol{nbin = 64, \rho = 0.03}$, $\mu_{rate} = \mathbf{2.0}, \mu = \mathbf{0.06}$, $\mu_{max} = \mathbf{10^5}$)

although foreground and background voxels have distinct values in the original image, choosing the threshold values from the noisy image may lead to misclassification in boundaries of the ellipse and deformable model may get trapped in the inner boundaries rather than outer edges of ROI.

5.2.1.2 RBF Interpolation for Mesh Initialization

Our initial mesh model for this experiment is a spherical mesh model expressed by

$$(\frac{x-50}{10})^2 + (\frac{y-50}{10})^2 + (\frac{z-50}{10})^2 = 1 \tag{5.3}$$

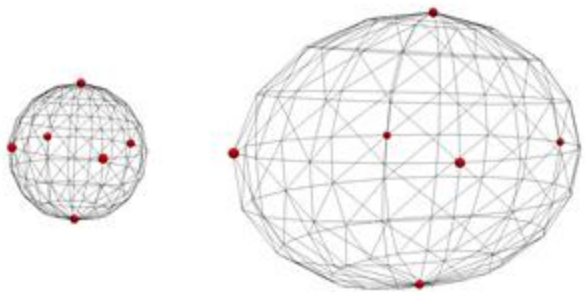

(a) (b)

Figure 5.4. RBF deformation (a) initial model (b) deformed model

	Number of mesh vertices	Number of mesh faces	Landmarks	TO	Er
RBF deformed (Registration only)	121	238	6	0.851	0.079
PDM coarse-to-fine segmentation				0.954	0.036
RBF deformed (Registration only)	941	1878	6	0.851	0.079
PDM coarse-to-fine segmentation				0.960	0.032

Table 5.1. Numerical results of our approach on ellipsoid represented by different levels of mesh complexity. The parameter set in 4.25 for first and second experiments are ($\boldsymbol{\alpha = 0.04, \beta = 0.07, \gamma = 1.0, \delta = 0.7}$) and ($\boldsymbol{\alpha = 0.02, \beta = 0.2, \gamma = 1.0, \delta = 0.7}$), correspondingly.

For registering the model to the image, we selected 6 control points from the model and their corresponding landmarks from the image and all these points are selected at the maxima of the model. The mesh model before and after RBF-deformation are depicted in Figure 5.4.

In this experiment, we chose a multiquadric kernel function ($\phi(r) = \sqrt{1 + r^2}$) which is used in most applications and in our case it showed better deformation than the other options. At this stage, the model is coarsely matched with the ROI i.e. the location of non-control points is automatically estimated by interpolation.

Although, RBF interpolation is a mesh-less deformation procedure, parametric deformable model requires the vertex normal vectors for evolution of the model towards the edges of ROI. Thus, after defamation the next step is to calculate the face and vertex normal vectors to assess the direction of evolution of the model.

5.2.1.3 Parametric Deformation Model for Coarse-to-Fine Segmentation

We conducted two experiments on two levels of mesh complexity. According to histogram acquired in preprocessing stage, the lower and upper thresholds were *0.8* and *1.0*, respectively. Table 5.1 displays the experimental data on the synthetic image. The table highlights the changes in overlapping measures after registration phase and PDM segmentation. According to the data, *TO* measure shows increase while misclassification error decreases significantly. Therefore, the

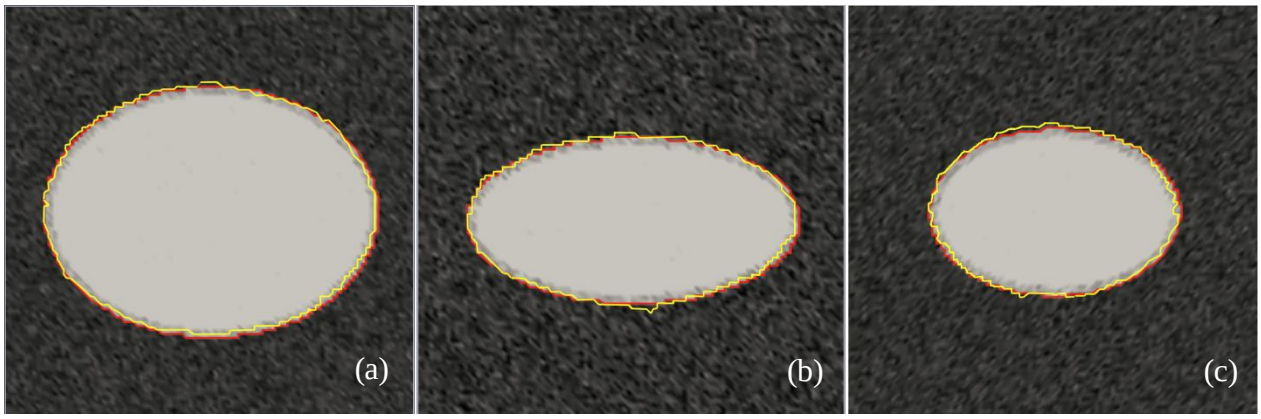

Figure 5.5. Segmentation of synthetic data from (a) coronal (b) sagittal (c) axial planes. Red and yellow contours denote GT data and result of segmentation by our methodology, respectively.

results are improved after increasing the number of mesh points so that the vertices are distributed evenly to handle concavities and convexities;

To show the accuracy of the framework, we showed the result of segmentation on sample 2D slices in Figure 5.5 Also, an overview of the segmentation of synthetic data is presented in Figure 5.6.

5.2.2. Segmentation of Proximal Femur from MR Images

In our study, the ROI is proximal femur that is decomposed to cortical and spongy tissues with different levels of hydrogen. As mentioned earlier, the difference in the amount of hydrogen in the tissues causes the tissues to appear with distinct intensity during the acquisition process. In MR images of femur, the cortical bone often shows up in black while the spongy tissue has gray-to-white intensity close to the intensity of fat.

We present the performance of the proposed framework on two sets of 3 Tesla (3T) MRI data

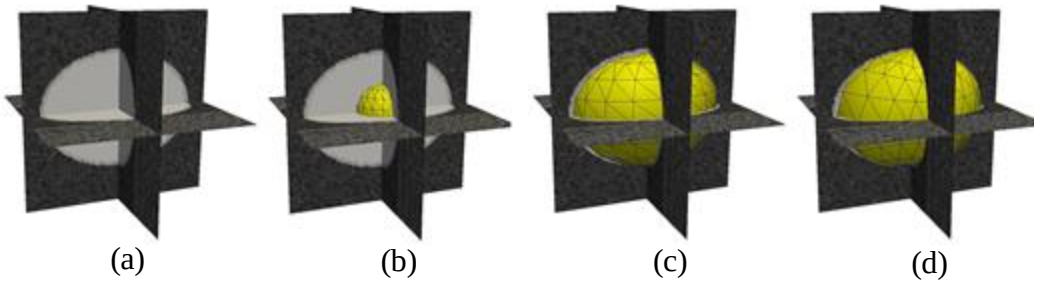

Figure 5.6. Overview of the process on synthetic data (a) Synthetic image containing an ellipsoid (b) Initial mesh model (c) RBF deformed mesh (Registration only) (d) PDM final segmentation

for segmentation of proximal femur from anisotropic and isotropic volumes. The first dataset consists of 33 images of 256×256 with single slice resolution of 0.81×0.81 with inter-slice distance of 3.25 mm so that the reconstructed volumetric image is anisotropic. The second dataset, however, constitutes 160 images of 256×256 with 0.89 inter-slice distance equal to single slice pixel dimensions and the 3D image is isotropic. Moreover, the GT data was segmented by the specialized musculoskeletal radiologist from 2D series and the results were voxelized to acquire 3D images.

In both experiments, a challenge with segmentation of the femur in MR images is in the shaft of the anatomy where the edges of spongy and cortical bones are close; the model may get attracted to spongy tissue boundaries rather than the outer surface of the cortical bone. This fact necessitates the existence of a region-based term in addition to gradient information to pass over the edge traps. The second challenge is associated with misclassification in the head of the femur where the thickness of the cortical bone is insignificant and intensity similarity between cartilage and spongy bone may give rise to over-segmentation or leakage into adjacent tissues. Another area where leakage is most probably to happen is intertrochanteric line; the bone is in adjacency with fat tissue of similar intensity and the edges are spurious.

5.2.2.1 Image Preprocessing

As stated earlier, a challenge with segmentation of MR images is the blurred edges which, leads to misclassification. Thus, in preprocessing step we have to choose the parameters in a way to eliminate false edges while preserve the obscure edges. The following figures show the result of preprocessing on each volume.

In both experiments, the thresholded balloon force is used to pass the model over spongy bone edges towards the outer surface of the cortical bone. As a result, the important threshold values that have to be extracted from the histogram are correspondent to the intensity of cortical bone.

Accordingly, the intensity range of the cortical bone is corresponding to the first peak in both figures that is approximately between *[0, 0.15]* for Dataset 1 (Figure 5.7) and *[0, 0.2]* for Dataset 2 (Figure 5.8). The results of filtering on the sample slices are indicated in Figure 5.9.

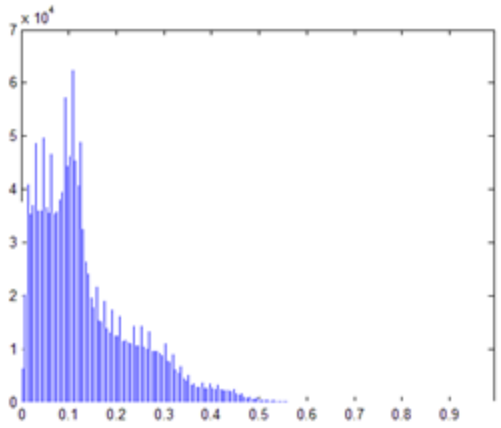

Figure 5.7. Histogram of Dataset 1 (a) original 3D volume (b) after preprocessing ($\boldsymbol{nbin = 64, \rho = 0.01}$, $\mu_{rate} = \mathbf{2.0}, \mu = \mathbf{0.02}$, $\mu_{max} = \mathbf{10^5}$)

5.2.2.2 RBF Interpolation for Mesh Initialization

We use an anatomical atlas mesh as the initial model which is semi-automatically registered on the 3D images by means of a multiquadric RBF-interpolation. Needless to say that choosing the sufficient number of effective control points from the model and accuracy in finding the corresponding landmarks is a task that can have direct influence on the final results. Especially, for objects with more concavities and convexities, enough number of points should be provided to install the model close enough to the boundaries of ROI.

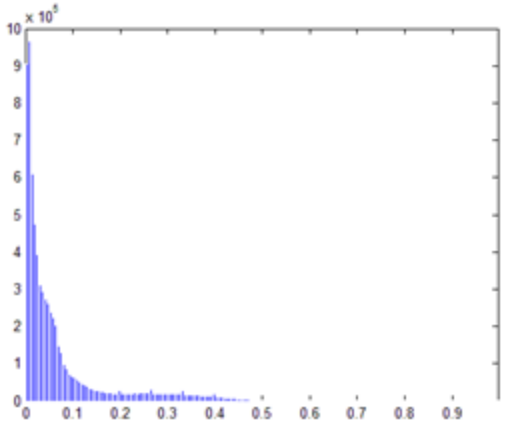

Figure 5.8. Histogram of Dataset 2 (a) original 3D volume (b) after preprocessing ($\boldsymbol{nbin = 64, \rho = 0.015}$, $\mu_{rate} = \mathbf{2.0}, \mu = \mathbf{0.03}$, $\mu_{max} = \mathbf{10^5}$)

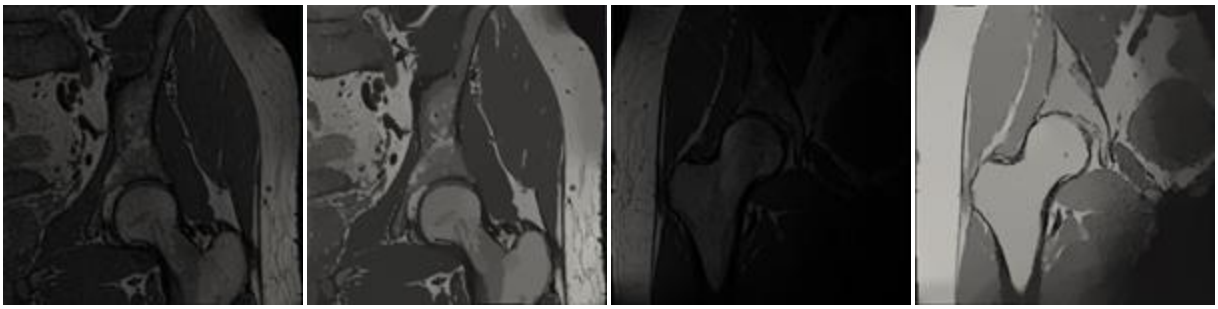

(a) (b) (c) (d)

Figure 5.9. Preprocessing results from sample slices (a) original image of Dataset 1 (b) preprocessed image (c) original image of Dataset 2 (d) preprocessed image

For deforming the model on Dataset 1 we used 17 points and for Dataset 2 we selected 23 points. Our strategy for point selection was to choose points in extrema and the points were the model was most likely to stray. The position of the control points and landmarks are depicted in Figure 5.10.

As the next step, we tessellated the mesh in order to increase the flexibility of the model in handling the object complexities; specifically, in trochanteric areas the model should be supplied by sufficient number of points to move the model towards the convex surface.

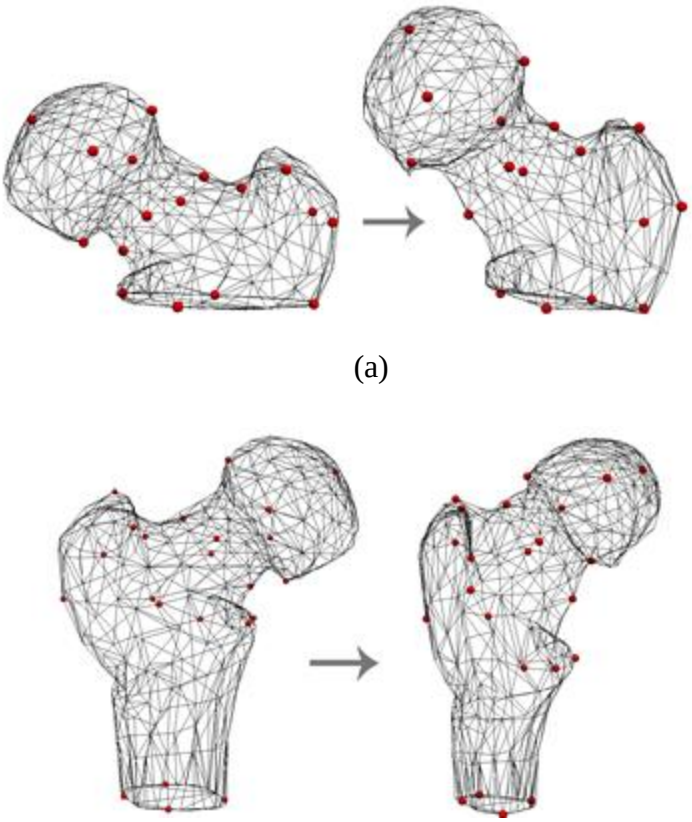

Figure 5.10. RBF deformation piecewise registration on clinical data by a multiquadric function (a) Atlas mesh model before and after registration on Dataset1 (b) atlas mesh model before and after registration on Dataset2

	Number of mesh vertices	Number of mesh faces	Number of landmarks	Elapsed time (/s)	TO	Er
Dataset 1						
RBF deformed (Registration only)	2330	4656	17	2.927	0.728	0.146
PDM coarse-to-fine segmentation					0.883	0.134
Dataset 2						
RBF deformed (Registration only)	2492	4980	23	2.950	0.761	0.173
PDM coarse-to-fine segmentation					0.883	0.102

Table 5.2. Quantitative results of our approach on clinical data

5.2.2.3 Parametric Deformation Model for Coarse-to-Fine Segmentation

Table 5.2 summarizes the preliminary analysis on Dataset 1 and Dataset 2. The experiments were perofrmed on a Core i7-3.40GHz processor with 16.0 GB of installed memory. The thresholds for external forces were chosen according to the section 5.2.2.1.

Following figures indicate the final results on the data from three planes. Due to space limitation, we selected three slices from each dataset from axial, sagittal and coronal views.

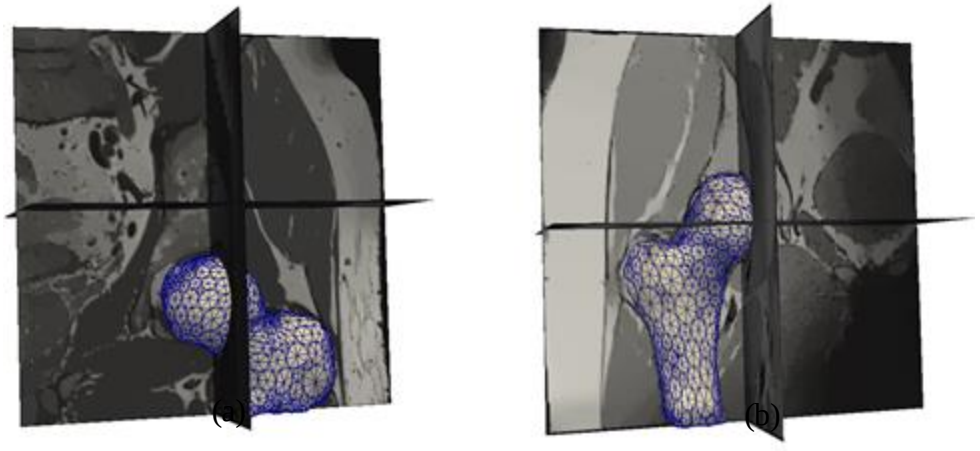

Figure 5.11. Segmentation of 3D volumes (a) Dataset 1 (b) Dataset 2

Comparatively, segmentation of Dataset 2 is more challenging since the image has remarkable inhomogeneity artifacts and due to variable thickness of the cortex along the length of the femur the mesh is likely to get attracted to the edges of spongy bone rather than cortical bone; withal, the balloon force prevents the shaft part of the mesh to shrink by means of applying a force in opposite direction to internal forces.

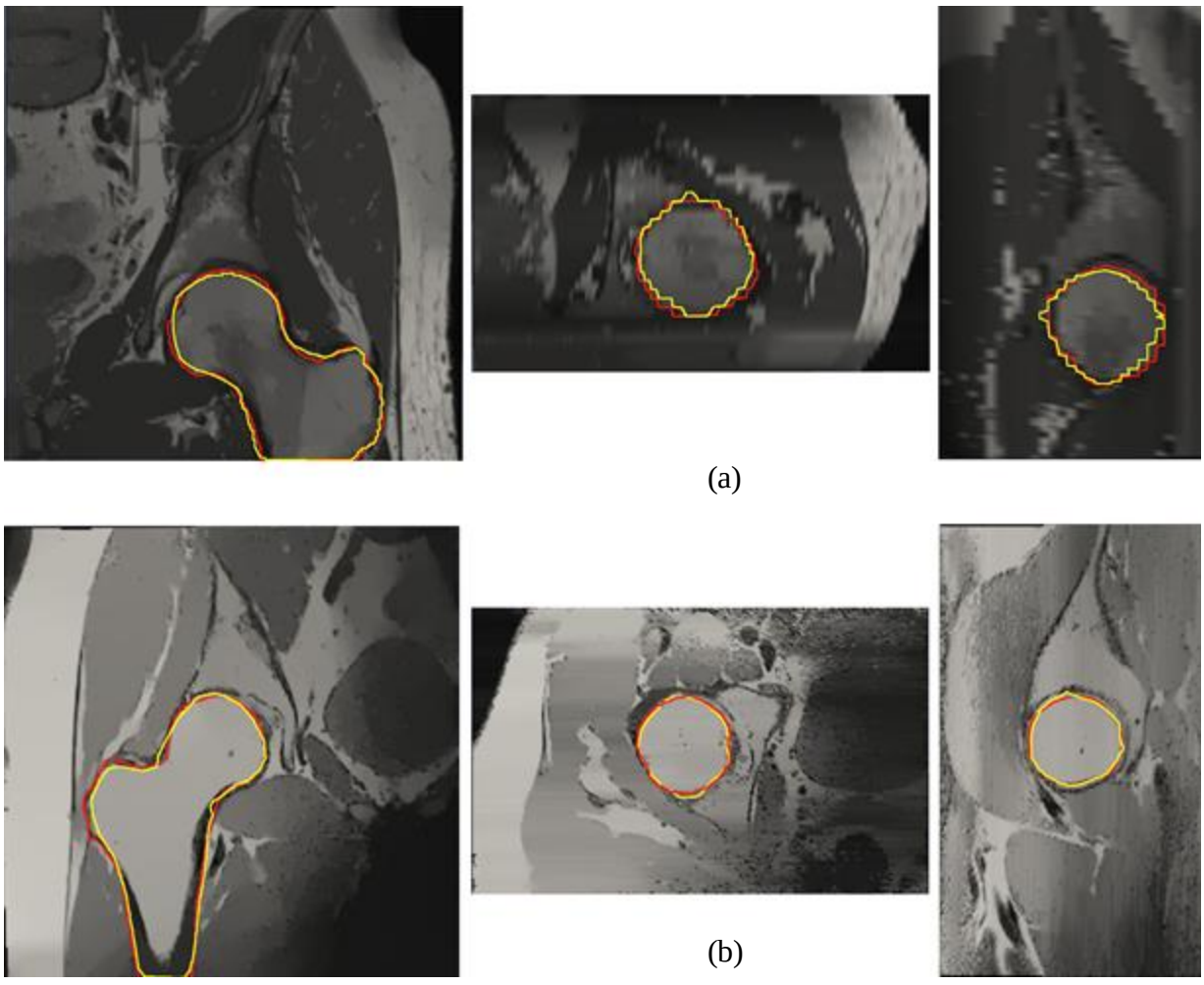

Figure 5.12. Results of our parametric deformable model segmentation framework from sampled coronal, axial, and sagittal planes (a) Dataset1 (b) DataSet2 (Red and yellow contours denote the ground truth data manually segmented by professional and results of our methodology, respectively). There is small difference between two pixelwise segmentations but our method shows robustness against leakage

5.3. Validation

In order to validate our results we compare the output of our method with related techniques in order to show how our method can improve the results of segmentation. These related techniques differ from our method in the definition of external forces; To put it another way, we have fixed the initial registered model as well as internal forces; so, in all experiments PDM is located close to the boundaries of ROI and internal forces have the same effect in all tests.

We compare the output of our segmentation scheme with the following technique:

- *Classical PDM*; as in Chapter 3, the forces is defined as

$$\overrightarrow{F_{Grad}}(v_i) = -\nabla\|\nabla I(v_i)\|. \tag{5.4}$$

  The forces works with intensity of the gradient image and the method takes advantage of edge information only.

- *Delingette's Gradient and Edge Forces* [134]*;* the definition of gradient force was presented in Chapter 3 in detail. Furthermore, the edge force is expressed as a force in the direction of the normal vector with respect to closest edge voxel; i.e.

$$\overrightarrow{F_{Edge}}(v_i^t) = e_i - v_i^t, \qquad i = 1, \dots, M. \tag{5.5}$$

  where e_i is the closest edge voxel to vertex $v_i$at time t.

- *Delingette's Gradient and Balloon Forces*; the external force is the sum of Delingette's gradient force and classical balloon force.

Table 5.3 illustrates the numerical results of segmentation with the aforementioned methods in comparison with our methodology. We compare the results by analyzing both measures. Accordingly, a good segmentation method is the one that increases *TO* and decreases *Er*. As indicated in the table classical PDM shows under-segmentation in both experiments because the evolution is dependent on the gradient of the image. The same argue is true about the second method; although it improves the results compared to the classical algorithm, the results still suffer from under-segmentation problem. On the contrary, the third method on both volumes shows an over-segmentation issue; the reason is that the balloon force inflates the model without any constraints that leads to leakage. However, we resolved this problem by applying the balloon

	Dataset 1			Dataset 2		
	TO	Er	Time(s)	TO	Er	Time(s)
Classical PDM	0.724	0.148	1.400	0.748	0.158	2.292
Delingette's Gradient and Edge Forces	0.781	0.155	2.786	0.795	0.125	2.748
Delingette's Gradient and Balloon Forces	0.914	0.148	2.894	0.954	0.153	2.848
Our Method	0.883	0.134	2.927	0.883	0.102	2.950

Table 5.3. Quantitative analysis of similar parametric deformable model segmentation algorithms on MR data images

force wherever some threshold constraint is satisfied and we have successfully improved the ROI segmentation in both volumes. The results of applying the algorithms from sample slices are depicted in Figure 5.13. As can be seen, the quantitative results totally confirm the visual results.

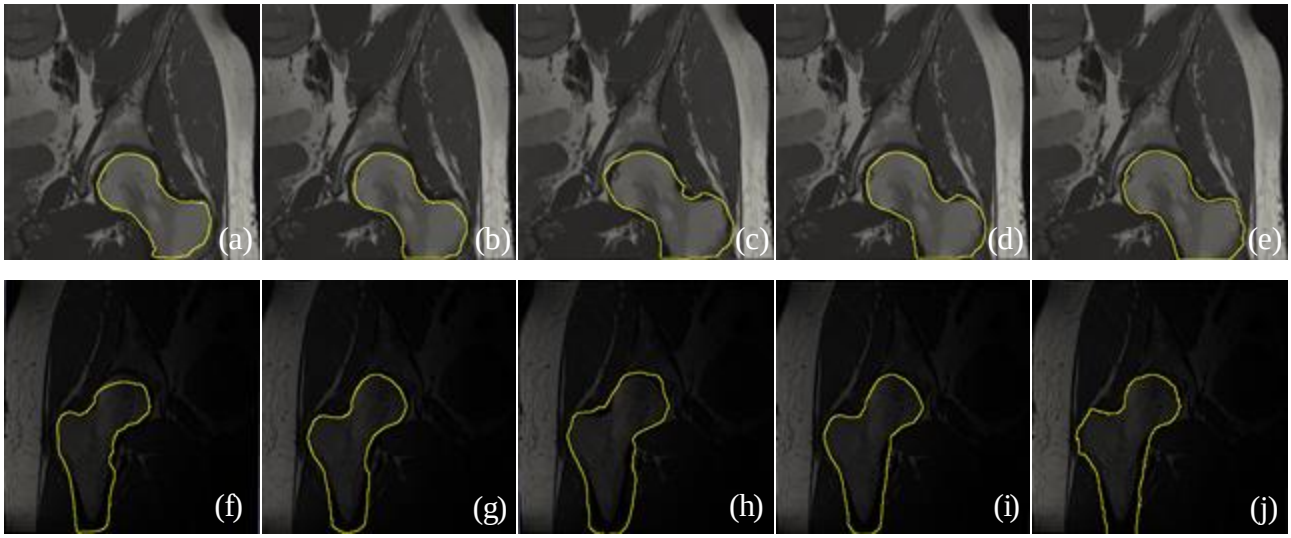

Figure 5.13. Results of segmentation on Dataset 1 and Dataset 2 from sample sagittal planes (a and f) Classical PDM, (b and g) Delingette's Gradient and Edge Forces, (c and h) Delingette's Gradient and Balloon Forces, (d and i) Our Method, (e and j) GT data

CHAPTER 6

Conclusion and Future Work

6.1. Conclusion

In this thesis, a 3D active model framework was proposed for segmenting proximal femur form MR images of hip. The technique is specifically useful for segmentation of objects with undesirable edges adjacent to the boundaries of ROI or obscure edges along ROI. Furthermore, the 3D scheme facilitates smooth and coherent inter-slice delineation of proximal femur. To put it another way, in comparison with reconstruction of 3D object from per-slice segmented ROI, the 3D approach is time effective and consecutive slices of the result are consistent.

With a two-phase pipeline, firstly, a model is piecewise registered to the preprocessed image by an RBF interpolator; secondly, the coarsely matched model evolves towards the edges of ROI under the influence of forces in order to refine the segmentation. In terms of the processing time, the first phase runs instantly and the second stage achieves a robust segmentation in a few seconds.

The initial model is an atlas triangular mesh model that is deformed in a point-by-point system. For launching the deformation function, user interaction is partially required to determine the displacement of a few points from the model and the position of the rest of the points are interpolated by solving a system.

The refinement module utilizes model explicit specifications and image properties to establish internal and external forces. The internal forces manage the connectivity of the vertices and external forces adjust the position of the model with respect to image properties; in particular, external forces use both boundary and regional properties to evolve the model.

The results demonstrate the robustness in rapid segmentation of 3D volumes of both high and low resolution images. The adoption reveals that method is not only applicable to proximal femur segmentation in MR images, but also extensible to various segmentation tasks with other structural or functional image modalities.

Despite of plausible results, a shortcoming of the technique is associated with the efficient initialization of the model to the image; i.e. the performance is dependent on the accuracy of the registration and user interaction and the accurate control point and landmark selection directly affect the performance of the parametric model deformation module.

6.2. Future Work

The proposed system can be improved in many aspects in future. First, the coarse matching phase can be substituted by an automatic procedure that is able to optimize the number and the position of points. Thus, the error of interactive landmark selection is expected to be decreased.

The second improvement is to empowering the user interaction by allowing the radiologist to manually adjust the position of the vertices before or after refinement in order to increase the performance of the system and providing better visual results for further analysis.

The third aspect of enhancement can be related to PDM for automatic parameter selection in order to control the effect of acting forces. However, automating the system may give rise to a trade-off between the speed and the performance.

Another option that can be added to the system is automatic calculation of the measures used for FAI diagnosis such as those mentioned in 2.4.1 and integrating the system with such options can increase its functionality.

References

[1] K. Rakhra, "MRI/CT in FAI," in *Femoroacetabular impingement*, Springer Berlin Heidelberg, 2012, pp. 41-55.

[2] P. Banerjee and C. Mclean, "Femoroacetabular impingement: a review of diagnosis and management," *Current Reviews in Musculoskeletal Medicine*, vol. 4, no. 1, pp. 23-32, 2011.

[3] H. Gray and W. Lewis, Anatomy of the human body, vol. 20, Philadelphia: Lea & Febiger, 1918, pp. 150-156.

[4] P. H. A. o. Canada, "It's Your Health," 2008. [Online]. Available: http://www.hc-sc.gc.ca/hl-vs/alt_formats/pacrb-dgapcr/pdf/iyh-vsv/diseases-maladies/seniors-aines-ost-art-eng.pdf.

[5] T. N. C. C. f. C. Conditions, "Osteoarthritis: national clinical guideline for care and management in adults," 2008. [Online]. Available: Available: http://www.nice.org.uk/nicemedia/pdf/CG059FullGuideline.pdf.

[6] K. Siebenrock and P. Henle, "X-Ray examination in FAI," in *Femoroacetabular Impingement*, Springer Berlin Heidelberg, 2012, pp. 31-39.

[7] P. Magill, J. Baker and K. Mulhall, "Femoroacetabular impingement," *The Open Sports Medicine Journal*, vol. 4, pp. 75-80, 2010.

[8] M. Umer, Y. Sepah, S. A. Asif and J. M. I., "Acetabular morphometry and prevalence of hip dysplasia in South Asian population," *Orthopedic reviews*, vol. 1, no. 1, 2009.

[9] J. Dettori, R. Hashimoto and E. Brodt, "Hip surgery procedures for treatment of femoroacetabular impingement syndrome," 2011. [Online]. Available: http://www.hta.hca.wa.gov/documents/fai_final_082611.pdf.

[10] J. Hornak, "Introduction," in *The Basics of MRI*, Interactive Learning Software, 2008.

[11] J. Rajapakse and F. Kruggel, "Segmentation of MR images with intensity inhomogeneities," *Image and Vision Computing*, vol. 16, no. 3, pp. 165-180, 1998.

[12] A. Hayashi, "Hip Resurfacing: A Boon for Boomers or Too Risky?," *American Association of Orthopaedic Surgeons,* vol. 7, no. 12, 2013.

[13] N. Otsu, "A threshold selection method from gray-level histograms," *IEEE Transactions on Systems, Man and Cybernetics,* vol. 9, no. 1, pp. 62-66, 1979.

[14] P. Kalavathi, "Brain tissue segmentation in MR brain images using multiple Otsu's thresholding technique," in *International Conference on Computer Science and Education (ICCSE)*, 2013.

[15] Y. Nakagawa and A. Rosenfeld, "Some experiments on variable thresholding," *Pattern Recognition,* vol. 11, no. 3, p. 191–204, 1979.

[16] J. Bersen, "Dynamic thresholding of grey-level images," in *International Conference on Pattern Recognition (ICPR),* Paris, 1986.

[17] C. K. Chow and T. Kaneko, "Automatic boundary detection of the left ventricle from cineangiograms," *Computers and Biomedical Research,* vol. 16, no. 5, pp. 388-410, 1972.

[18] J. Zhang, C. Yan, C. Chui and S. Ong, "Fast segmentation of bone in CT images using 3D adaptive thresholding," *Computers in Biology and Medicine,* vol. 40, no. 2, pp. 231-236, 2010.

[19] M. Moussallem, P. Valette, A. Traverse-Glehen, C. Houzard, C. Jegou and F. Giammarile, "New strategy for automatic tumor segmentation by adaptive thresholding on PET/CT images," *Applied Clinical Medical Physics,* vol. 13, no. 5, 2012.

[20] S. Park, J. H. Kim, S. Lee and K. K.G., "Comparative assessment of 3D region growing methods for lung airway segmentation : evaluation with pathological and normal cases," *World Congress on Medical Physics and Biomedical Engineering,* vol. 14, pp. 2525-2527, 2006.

[21] N. Mešanović, M. Grgić, H. Huseinagić, M. Maleš, E. Skejić and M. Smajlović, "Automatic CT image segmentation of the lungs with region growing algorithm," in *International Conference on Systems, Signals and Image Processing,* 2011.

[22] K. Chang, H. Zhang, S. Chen and L. Chen, "Automatic colon sgmentation uing iolated-cnnected treshold," in *International Conference on Robot, Vision and Signal Processing*

(RVSP), 2011.

[23] S. Sivaperumal and M. Sundhararajan, "Brain tumor analysis for MRI image segmentation using seaded region growing and PCNN," *International Journal of Electronics, Communication & Instrumentation Engineering Research and Development (IJECIERD)*, vol. 3, no. 2, pp. 175-182, 2013.

[24] A. Aboaba, S. Hameed, O. Khalifa and A. Abdalla, "Computational hybrid level-set and region growing techniques: a strategy for 3D fast segmentation of medical images," in *International Conference on Instrumentation,Communication, Information Technology and Biomedical Engineering*, 2011.

[25] E. Zanaty and A. Afifi, "A watershed approach for improving medical image segmentation," *Journal of Computer Methods Biomechanical and Biomedical Engineering*, 2012.

[26] A. EL Allaoui and M. Nasri, "Threshold optimization by genetic algorithm for segmentation of medical images by region growing," *International Journal of Emerging Trends and Technology in Computer Science (IJETTCS)*, vol. 1, no. 2, pp. 161-166, 2012.

[27] J. Yan, B. Zhao, L. Wang, A. Zelenetz and L. Schwartz, "Marker-controlled watershed for lymphoma segmentation in sequential CT images," *Medical Physics*, vol. 33, no. 7, pp. 2452-2460, 2006.

[28] S. Delest, R. Bone and H. Cardot, "Automatically computed markers for the 3D watershed segmentation," in *IEEE International Conference on Image Processing (ICIP)*, 2007.

[29] M. A. Gonzalez and V. Ballarin, "Automatic marker determination algorithm for watershed segmentation using clustering," *Latin American Applied Research*, vol. 39, no. 3, 2009.

[30] S. Salman and A. A. Bahrani, "Segmentation of tumor tissue in gray medical images using watershed transformation method," *Computer Science and Applied Mathematics*, vol. 2, no. 4, pp. 123-127, 2010.

[31] M. Mancas and B. Gosselin, "Towards an automatic tumor segmentation using iterative

watersheds," in *Medical Imaging Conference of the International Society for Optical Imaging (SPIE Medical Imaging),* 2004.

[32] V. Grau, A. Mewes, M. Alcaniz, R. Kikinis and S. Warfield, "Improved watershed transform for medical image segmentation using prior information," *IEEE Transactions on Medical Imaging,* vol. 23, no. 4, pp. 447 - 458, 2004.

[33] K. Haris, S. Efstratiadis, N. Maglaveras and A. Katsaggelos, "Hybrid image segmentation using watersheds and fast region merging," *IEEE Transactions on Image Processing,* vol. 7, no. 12, pp. 1684 - 1699, 1998.

[34] R. Lapeer, A. Tan and A. Aldridge, "Active watersheds: combining 3D watershed segmentation and active contours to extract abdominal organs from MR images," in *International Conference on Medical Image Computing and Computer-Assisted Intervention,* 2002.

[35] Y. Huang and D. Chen, "Watershed segmentation for breast tumor in 2-D sonography," *Ultrasound in Medicine & Biology,* vol. 30, no. 5, p. 625–632, 2004.

[36] M. Ahmed, S. Yamany, N. Mohamed, A. Farag and T. Moriarty, "A modified fuzzy c-means algorithm for bias field estimation and segmentation of MRI data," *IEEE Transactions on Medical Imaging,* vol. 21, no. 3, pp. 193-199, 2002.

[37] K. Chuang, H. Tzeng, S. Chen, J. Wu and T. Chen, "Fuzzy C-means clustering with spatial information for image segmentation," *Computerized Medical Imaging and Graphics,* vol. 30, no. 1, pp. 9-15, 2006.

[38] P. Vasuda and S. Satheesh, "Improved fuzzy C-means algorithm for MR brain image segmentation," *International Journal on Computer Science and Engineering (IJCSE),* vol. 2, no. 5, pp. 1713-1715, 2010.

[39] N. Abdul Khalid, S. Ibrahim and P. Haniff, "MRI brain abnormalities segmentation using K-Nearest Neighbors (k-NN)," *International Journal on Computer Science and Engineering (IJCSE),* vol. 3, no. 2, pp. 980-990, 2011.

[40] S. Dalmiya, A. Dasgupta and S. Kanti Datta, "Application of Wavelet based K-means Algorithm in Mammogram Segmentation," *International Journal of Computer*

Applications, vol. 52, no. 15, pp. 15-19, 2012.

[41] X. Zhang, C. Zhang, W. Tang and Z. Wei, "Medical image segmentation using improved FCM," *Science China Information Sciences,* vol. 55, no. 5, pp. 1052-1061, 2012.

[42] A. Jain, M. Murty and P. Flynn, "Data clustering: a review," *ACM Computing Surveys (CSUR),* vol. 31, no. 3, pp. 264-323, 1999.

[43] P. Vijayalakshmi, K. Selvamani and M. Geetha, "Segmentation of brain MRI using K-means clustering algorithm," *International Journal of Engineering Trends and Technology,* pp. 113-115, 2011.

[44] K. Somasundaram, S. Vijayalakshmi and T. Kalaiselvi, "Segmentation of brain MRI using K-means clustering algorithm," *International Journal of Computational Intelligence and Informatics,* vol. 1, no. 1, pp. 75-79, 2011.

[45] J. Bezdek, Pattern Recognition with fuzzy objective function algorithms, New York: Plenum Press, 1981.

[46] M. Al-Zoubi, A. Hudaib and B. Al-Shboul, "A fast fuzzy clustering algorithm," *International Conference on Artificial Intelligence, Knowledge Engineering and Data Bases,* vol. 6, pp. 28-32, 2007.

[47] Y. Li and G. Li, "Fast fuzzy C-Means clustering algorithm with spatial constraints for image segmentation," in *Advances in Neural Network Research and Applications*, Springer Berlin Heidelberg, 2010, pp. 431-438.

[48] R. Krishnapuram and J. Keller, "The possibilistic C-Means algorithm: insights and recommendations," *IEEE Transactions on Fuzzy Sytems,* vol. 4, no. 3, pp. 385-393, 1996.

[49] A. Rajendran and R. Dhanasekaran, "Enhanced possibilistic fuzzy C-means algorithm for normal and pathological brain tissue segmentation on magnetic resonance brain image," *Arabian Journal for Science and Engineering,* vol. 38, no. 9, pp. 2375-2388, 2013.

[50] M. Shasidhar, V. Raja and B. Kumar, "MRI brain image segmentation using modified fuzzy C-means clustering algorithm," in *International Conference on Communication Systems and Network Technologies (CSNT)*, Katra, Jammu, 2011.

[51] A. Dasgupta, "Demarcation of brain tumor using modified fuzzy C-means,"

International Journal of Engineering Research and Applications, vol. 2, no. 4, pp. 529-533, 2012.

[52] S. Kannan, S. Ramathilagam and R. Pandiyarajan, "Modified bias field fuzzy C-means for effective segmentation of brain MRI," in *Transactions on Computational Science VIII*, Springer Berlin Heidelberg, 2011, pp. 127-145.

[53] D. Pham and J. Prince, "An adaptive fuzzy C-means algorithm for image segmentation in the presence of intensity inhomogeneities," *Pattern Recognition Letters,* vol. 20, no. 1, pp. 57-68, 1999.

[54] D. Wankai, X. Wei, P. Chao and L. Jianguo, "MRI brain tumor segmentation based on improved fuzzy c-means method," in *SPIE*, 2009.

[55] A. Goldberg and R. Tarjan, "A new approach to the maximum flow problem," in *ACM symposium on Theory of computing*, 1986.

[56] L. Ford and D. Fulkerson, "Maximal flow through a network," *Canadian Journal of Mathematics* , vol. 8, p. 399–404, 1956.

[57] L. Kantorovich, "A new method for solving some classes of extremal problems," *Doklady Acad Sci USSR,* vol. 28, pp. 211-14, 1940.

[58] J. Orlin, "Max flows in O(nm) time, or better," in *ACM symposium on Symposium on theory of computing*, 2013.

[59] Y. Boykov and M. Jolly, "Interactive graph cuts for optimal boundary and region segmentation of objects in N-D images," in *International Conference on Computer Vision (ICCV)*, 2001.

[60] Y. Boykov and G. Funka-Lea, "Graph cuts and efficient N-D image segmentation," *International Journal of Computer Vision,* vol. 70, no. 2, pp. 109-131, 2006.

[61] V. Chen and S. Ruan, "Graph cut segmentation technique for MRI brain tumor extraction," in *International Conference on Theory Tools and Applications (IPTA)*, Paris, 2010.

[62] I. Despotović, I. Segers, L. Platisa, E. Vansteenkiste, A. Pizurica, K. Deblaere and W. Philips, "Automatic 3D graph cuts for brain cortex segmentation in patients with focal

cortical dysplasia," in *International Conference of the IEEE Engineering in Medicine and Biology Society(EMBC)*, Boston, 2011.

[63] G. Slabaugh and G. Unal, "Graph cuts segmentation using an elliptical shape prior," in *IEEE International Conference on Image Processing*, 2005.

[64] O. Veksler, "Star shape prior for graph-cut image segmentation," in *European Conference on Computer Vision*, Marseille, 2008.

[65] P. Das, O. Vekslera, V. Zavadsky and Y. Boykov, "Semiautomatic segmentation with compact shape prior," *Image and Vision Computing*, vol. 27, no. 1-2, pp. 206-219, 2009.

[66] D. Freedman and T. Zhang, "Interactive graph cut based segmentation with shape priors," in *IEEE Computer Society Conference on Computer Vision and Pattern Recognition (CVPR)*, 2005.

[67] D. Grosgeorgea, C. Petitjeana and S. Ruan, "Graph cut segmentation with a statistical shape model in cardiac MRI," *Computer Vision and Image Understanding*, vol. 117, no. 9, p. 1027–1035, 2013.

[68] T. Cootes, C. Taylor, D. Cooper and J. Graham, "Active shape models-their training and application," *Computer Vision and Image Understanding*, vol. 61, no. 1, p. 38–59, 1995.

[69] T. Cootes, G. Edwards and C. Taylor, "Active appearance models," in *European Conference on Computer Vision*, Freiburg, 1998.

[70] E. Angelini, Y. Jin and A. Laine, "State of the art of level set methods in segmentation and registration of medical imaging modalities," in *Handbook of Biomedical Image Analysis*, Springer US, 2005, pp. 47-101.

[71] J. Stanier, I. Bloch and M. Goldberg, "Segmentation schemes for knowledge-based construction of individual atlases from slice-type medical images," in *SPIE , Medical Imaging*, Newport Beach, 1993.

[72] X. Zhoua, T. Kitagawaa, K. Okuoa, T. Haraa, H. Fujitaa, R. Yokoyamab, M. Kanematsub and H. Hoshib, "Construction of a probabilistic atlas for automated liver segmentation in non-contrast torso CT images," *International Congress Series*, vol. 1281, p. 1169–1174, 2005.

[73] O. Commowick, V. Grégoire and G. Malandain, "Atlas-based delineation of lymph node levels in head and neck computed tomography images," *Radiotherapy and Oncology:Journal of the European Society for Radiotherapy and Oncology,* vol. 87, no. 2, pp. 281-289, 2008.

[74] F. Shi, P. Yap, Y. Fan, J. Gilmore, W. Lin and D. Shen, "Construction of multi-region-multi-reference atlases for neonatal brain MRI segmentation," *NeuroImage,* vol. 51, no. 2, pp. 684-693, 2010.

[75] B. Zitová and J. Flusser, "Image registration methods: a survey," *Image and Vision Computing,* vol. 21, no. 11, p. 977–1000, 2003.

[76] N. Alpert, D. Berdichevsky, Z. Levin, E. Morris and A. Fischman, "Improved methods for image registration," *NeuroImage,* vol. 3, no. 1, pp. 10-18, 1996.

[77] J. Maintz and M. Viergever, "A survey of medical image registration," *Medical Image Analysis,* vol. 2, no. 1, pp. 1-36, 1998.

[78] S. Bourouis, K. Hamrouni and N. Betrouni, "Automatic MRI brain segmentation with combined atlas-based classification and level-set approach," in *Image Analysis and Recognition*, Springer Berlin Heidelberg, 2008, pp. 770-778.

[79] A. Fedorov, X. Li, K. Pohl, S. Bouix, M. Styner, M. Addicott, C. Wyatt, D. J.B., W. Wells and R. Kikinis, "Atlas-guided segmentation of vervet monkey brain MRI," *The open neuroimaging journal,* vol. 5, pp. 186-197, 2011.

[80] J. Morin, C. Desrosiers and L. Duong, "Atlas-based segmentation of brain magnetic resonance imaging using random walks," in *IEEE Computer Society Conference on Computer Vision and Pattern Recognition Workshops (CVPRW)*, 2012.

[81] X. Zhuang, D. Hawkes, W. Crum, R. Boubertakh, S. Uribe, D. Atkinson, P. Batchelor, T. Schaeffter, R. Razavi and D. L. G. Hill, "Robust registration between cardiac MRI images and atlas for segmentation propagation," in *SPIE, Medical Imaging*, San Diego, 2008.

[82] J. Ulén, P. Strandmark and F. Kahl, "Optimization for multi-region segmentation of cardiac MRI," in *Statistical Atlases and Computational Models of the Heart, Imaging and*

Modelling Challenges, Springer Berlin Heidelberg, 2012, pp. 129-138.

[83] A. Gubern-Mérida, M. Kallenberg, R. Martí and N. Karssemeijer, "Multi-class probabilistic atlas-based segmentation method in breast MRI," in *Pattern Recognition and Image Analysis*, Springer Berlin Heidelberg, 2011, pp. 660-667.

[84] C. Ortiz and A. Martel, "Automatic atlas-based segmentation of the breast in MRI for 3D breast volume computation," *Medical Physics*, vol. 39, no. 10, pp. 5835-5848, 2012.

[85] Y. Gao and A. Tannenbaum, "Combining Atlas and Active Contour for Automatic 3D Medical Image Segmentation," in *IEEE International Symposium on Biomedical Imaging*, 2011.

[86] R. Kohavi, "A study of cross-validation and bootstrap for accuracy estimation and model selection," in *International Joint Conference on Artificial Intelligence*, 1995.

[87] J. Fürnkranz, "Pruning algorithms for rule learning," *Machine Learning*, vol. 27, no. 2, pp. 139-172, 1997.

[88] H. Chen, A. Cohn and X. Yao, "Ensemble learning by negative correlation learning," in *Ensemble Machine Learning*, Springer US, 2012, pp. 182-187.

[89] L. Prechelt, "Early stopping — but when?," in *Neural Networks: Tricks of the Trade*, Springer Berlin Heidelberg, 2012, pp. 53-67.

[90] X. Zhu, "Semi-supervised learning literature lurvey," Computer Sciences Technical Report 1530, 2006.

[91] T. Kohonen, "The self-organizing map," *Biological Cybernetics*, vol. 78, no. 9, pp. 1464 - 1480, 1990.

[92] J. Alirezaie, M. Jernigan and C. Nahmias, "Automatic segmentation of cerebral MR images using artificial neural networks," *IEEE Transactions on Nuclear Science*, vol. 45, no. 4, pp. 2174 - 2182, 2002.

[93] C. Chuang, C. P.E., M. Liou, C. Liou and Y. Kuo, "Application of self-organizing map (SOM) for cerebral cortex reconstruction," *International Journal of Computational Intelligence Research*, vol. 3, no. 1, pp. 32-36, 2007.

[94] J. Zhang and D. Da, "A multi-scale dynamically growing hierarchical self-organizing

sap for brain MRI image segmentation," *Advances in Neural Networks,* vol. 4492, pp. 1081-1089, 2007.

[95] T. Logeswari and M. Karnan, "Hybrid self organizing map for improved implementation of brain MRI segmentation," in *International Conference on Signal Acquisition and Processing(ICSAP),* Bangalore, 2010.

[96] A. Manduca, P. Christy and R. Ehman, "Neural network diagnosis of avascular necrosis from magnetic resonance images," in *SPIE*, 1993.

[97] H. Lan, T. Chang, W. Liao, Y. Chung and P. Chung, "Knee MR image segmentation combining contextual constrained neural network and level set evolution," in *IEEE Conference on Computational Intelligence in Bioinformatics and Computational Biology*, 2009.

[98] N. Long, D. Jiang and C. Ding, "Application of artificial neural networks in automatic cartilage segmentation," in *International Workshop on Advanced Computational Intelligence (IWACI),* Suzhou, Jiangsu, 2010.

[99] M. Kass, A. Witkin and D. Terzopoulos, "Snakes: active contour models," *International Journal of Computer Vision,* vol. 1, no. 4, pp. 321-331, 1988.

[100] D. Terzopoulos and K. Fleischer, "Deformable models," *The Visual Computer,* vol. 4, pp. 306-331, 1988.

[101] R. Malladi, J. Sethian and B. Vemuri, "Shape modeling with front propagation: a level set approach," *IEEE Transactions on Pattern Analysis and Machine Intelligence,* vol. 17, no. 2, pp. 158 - 175, 1995.

[102] V. Caselles, R. Kimmel and G. Sapiro, "Geodesic active contours," *International Journal of Computer Vision,* vol. 22, no. 1, pp. 61 - 79, 1997.

[103] T. McInerney and D. Terzopoulos, "Deformable models in medical image analysis: a survey," *Medical Image Analysis,* vol. 1, no. 2, p. 91–108, 1996.

[104] S. Osher and N. Paragios, Geometric level set methods in imaging, vision, and graphics, 1st ed., Springer, 2003.

[105] C. Baillard, P. Hellier and C. Barillot, "Segmentation of brain 3D MR images using

level sets and dense registration," *Medical Image Analysis,* vol. 5, no. 3, p. 185–194, 2001.

[106] O. Colliot, T. Mansi, N. Bernasconi, V. Naessens, D. Klironomos and A. Bernasconi, "Segmentation of focal cortical dysplasia lesions on MRI using level set evolution," *NeuroImage,* vol. 32, no. 4, p. 1621–1630, 2006.

[107] A. Bosnjak, G. Montilla, R. Villegas and I. Jara, "3D segmentation with an application of level set-method using MRI volumes for image guided surgery.," in *International Conference of the IEEE Engineering in Medicine and Biology Society (EMBS)*, Lyon, 2007.

[108] D. Rivest-Hénaultr and M. Cheriet, "Unsupervised MRI segmentation of brain tissues using a local linear model and level set," *Magnetic Resonance Imaging,* vol. 29, no. 2, p. 243–259, 2011.

[109] Z. Zhou, J. You, P. Heng and D. Xia, "Cardiac MR image segmentation and left ventricle surface reconstruction based on level set method," *Studies in Health Technology and Informatics,* vol. 111, pp. 629-632, 2005.

[110] K. Fritscher, R. Pilgram and R. Schubert, "Automatic cardiac 4D segmentation using level sets," in *Functional Imaging and Modeling of the Heart*, vol. 3504, Springer Berlin Heidelberg, 2005, pp. 113-122.

[111] S. Dakua and J. Sahambi, "A level set method for cardiac magnetic resonance image segmentation: an adaptive approach," in *International Conference on Industrial and Information Systems (ICIIS)*, Kharagpur, 2008.

[112] K. Cheng, L. Gu, J. Wu, W. Li and J. Xu, "A novel level set based shape prior method for liver segmentation from MRI images," *Medical Imaging and Augmented Reality,* vol. 5128, pp. 150-159, 2008.

[113] E. Goceri, M. Unlu, C. Guzelis and O. Dicle, "An automatic level set based liver segmentation from MRI data sets," in *International Conference on Image Processing Theory, Tools and Applications (IPTA)*, Istanbul, 2012.

[114] D. Terzopoulos, J. Platt, A. Barr and K. Fleischer, "Elastically deformable models," in *Computer Graphics and Interactive Techniques*, 1987.

[115] P. Radeva, J. Serrat and E. Marti, "A snake for model-based segmentation," in *International Conference on Computer Vision*, 1995.

[116] J. Pardoa, D. Cabelloa and J. Herasb, "A snake for model-based segmentation of biomedical images," *Pattern Recognition Letters*, vol. 18, no. 14, p. 1529–1538, 1997.

[117] C. Chesnaud, P. Refregier and V. Boulet, "Statistical region snake-based segmentation adapted to different physical noise models," *IEEE Transactions on Pattern Analysis and Machine Intelligence*, vol. 21, no. 11, pp. 1145 - 1157, 1999.

[118] L. Ji and H. Yan, "Robust topology-adaptive snakes for image segmentation," *Image and Vision Computing*, vol. 20, no. 2, p. 147–164, 2002.

[119] S. Lama and C. Tong, "Enhanced snake algorithm by embedded domain transformation," *Pattern Recognition*, vol. 39, no. 9, p. 1566–1574, 2006.

[120] O. Colliot, O. Camara and I. Bloch, "Integration of fuzzy spatial relations in deformable models-application to brain MRI segmentation," *Pattern Recognition*, vol. 39, no. 8, p. 1401–1414, 2006.

[121] I. Dagher and K. El Tom, "WaterBalloons: hybrid watershed balloon snake segmentation," *Image and Vision Computing*, vol. 26, no. 7, p. 905–912, 2008.

[122] H. Delingette, M. Hebert and K. Ikeuchi, "Image segmentation and shape representation using deformable surfaces," in *IEEE Computer Society Conference on Computer Vision and Pattern Recognition*, 1991.

[123] I. Cohen, N. Ayache and L. Cohen, "Segmenting, visualizing and characterizing 3D anatomical structures with deformable surfaces," in *International Conference of the IEEE Engineering in Medicine and Biology Society*, 1991.

[124] L. Cohen and I. Cohen, "Finite-element methods for active contour models and balloons for 2-D and 3-D images," *IEEE Transactions on Pattern Analysis and Machine Intelligence*, vol. 15, no. 11, pp. 1131 - 1147, 1993.

[125] T. McInerney and D. Terzopoulos, "Medical image segmentation using topologically adaptable surfaces," in *International Conference on Computer Vision, Virtual Reality and Robotics in Medicine*, 1995.

[126] T. McInerney and D. Terzopoulos, "Topology adaptive deformable surfaces for medical image volume segmentation," *IEEE Transactions on Medical Imaging,* vol. 18, no. 10, pp. 840-850, 1999.

[127] A. Alfiansyah, K. Ng and R. Lamsudin, "Deformable model for serial ultrasound images segmentation: application to computer assisted hip athroplasty," in *International Conference on Biomedical Engineering (IFMBE),* 2009.

[128] L. Cohen, "On active contour models and balloons," *CVGIP: Image Understanding,* vol. 53, no. 2, p. 211–218, 1991.

[129] M. Bakos, P. Karch and O. Dulova, "Advanced initialization possibilities of active contours," in *IEEE International Symposium on Applied Machine Intelligence and Informatics (SAMI),* 2012.

[130] S. Rahnamayan, H. Tizhoosh and M. Salama, "Automated snake initialization for the segmentation of the prostate in ultrasound images," *Image Analysis and Recognition,* vol. 3656, pp. 930-937, 2005.

[131] L. Xu, C. Lu, Y. Xu and J. Jia, "Image smoothing via L0 gradient minimization," *ACM Transactions on Graphics (TOG),* vol. 30, no. 6, 2011.

[132] H. Delingette, "General object reconstruction based on simplex meshes," *International Journal of Computer Vision,* vol. 32, no. 2, pp. 111-146, 1999.

[133] J. Mille, R. Bone, P. Makris and H. Cardot, "Segmentation and tracking of the left ventricle in 3D MRI sequences using an active surface model," in *IEEE International Symposium on Computer-Based Medical Systems(CBMS),* Maribor, 2007.

[134] J. Tohka, "Surface extraction from volumetric images using deformable meshes: a comparative study," in *European Conference on Computer Vision (ECCV),* 2002.

[135] C. M. Nambakhsha, J. Yuanb, K. Punithakumarc, a. Goelaa, M. Rajchla, T. Petersa and I. B. Ayeda, "Left ventricle segmentation in MRI via convex relaxed distribution matching," *Medical Image Analysis,* vol. 17, no. 8, p. 1010–1024, 2013.

[136] J. Schmid and N. Magnenat-Thalmann, "MRI bone segmentation using deformable models and shape priors," *International Conference on Medical Image Computing and*

Computer-Assisted Intervantion, vol. 11, no. 1, pp. 119-126, 2008.

[137] D. Pham, C. Xu and J. Prince, "Current methods in medical image segmentation," *Annual Review of Biomedical Engineering,* vol. 2, pp. 315-337, 2000.

[138] K. Noor Elaiza Abdul, I. Shafaf and H. Puteri Nurain Megat Mohd, "MRI brain abnormalities segmentation using k-Nearest Neighbors (k-NN)," *International Journal on Computer Science and Engineering,* vol. 3, no. 2, pp. 980-990, 2011.

[139] L. Lorigo, O. Faugeras, W. Grimson, R. Keriven and R. Kikinis, "Segmentation of bone in clinical knee MRI using texture-based geodesic active contours," *International Conference on Medical Image Computing and Computer-Assisted Intervention,* vol. 1496, pp. 1195-1204, 1998.

[140] Y. Hata and S. Kobashi, "Fuzzy segmentation of endorrhachis in magnetic resonance images and its fuzzy maximum intensity projection," *Applied Soft Computing* , vol. 9, no. 3, pp. 1156-1169, 2009.

[141] G. Hamarneh and X. Li, "Watershed segmentation using prior shape and appearance knowledge," *Image and Vision Computing,* vol. 27, no. 1-2, p. 59–68, 2009.

[142] J. Fripp, P. Bourgeat, S. Crozier and S. Ourselin, "Segmentation of the bones in MRIs of the knee using phase, magnitude, and shape information," *Academic Radiology,* vol. 14, no. 10, pp. 1201-1208, 2007.

[143] A. Frangia, M. Egmont-Petersenb, W. Niessena, J. Reiberb and M. Viergever, "Bone tumor segmentation from MR perfusion images with neural networks using multi-scale pharmacokinetic features," *Image and Vision Computing,* vol. 19, no. 9-10, p. 679–690, 2001.

[144] J. Carballido-Gamio, S. Belongie and S. Majumdar, "Normalized cuts in 3-D for spinal MRI segmentation," *IEEE Transactions on Medical Imaging,* vol. 23, no. 1, pp. 36-44, 2004.

[145] Y. Boykov and V. Kolmogorov, "An experimental comparison of min-cut/max- flow algorithms for energy minimization in vision," *IEEE Transactions on Pattern Analysis and Machine Intelligence,* vol. 26, no. 9, pp. 1124-1137, 2004.

[146] P. Anbeek, K. Vincken, F. Groenendaal, A. Koeman, M. van Osch and J. van der Grond, "Probabilistic brain tissue segmentation in neonatal magnetic resonance imaging," *Pediatric Research,* vol. 63, no. 2, pp. 158-163, 2008.

[147] S. Ababneh, J. Prescott and M. Gurcan, "Automatic graph-cut based segmentation of bones from knee magnetic resonance images for osteoarthritis research," *Medical Image Analysis,* vol. 15, no. 4, pp. 438-448, 2011.

[148] D. Zhang and S. Chen, "A novel kernelized fuzzy c-means algorithm with application in medical image segmentation," *Artificial Intelligence in Medicine,* vol. 32, no. 1, pp. 37-50, 2004.

[149] C. Ramirez, R. Enseñat and F. Mas, "Acquisition and digital images processing, comparative analysis of FPGA, DSP, PC for the subtraction and thresholding," in *Image Processing*, Y. Chen, Ed., InTech, 2009.

[150] M. Li, T. Huang and G. Zhu, "Improved fast fuzzy C-Means algorithm for medical MR images segmentation," in *International Conference on Genetic and Evolutionary Computing*, Hubei, 2008.

[151] H. Seim, D. Kainmueller, H. Lamecker, M. Bindernagel, J. Malinowski and S. Zachow, "Model-based auto-segmentation of knee bones and cartilage in MRI data," in *MICCAI Workshop Medical Image Analysis for the Clinic*, 2010.